Localization of Deformation in Thin Shells under Indentation

by

Alice M. Nasto

B.A., University of Chicago (2011)

Submitted to the Department of Mechanical Engineering
in partial fulfillment of the requirements for the degree of

Master of Science

at the

MASSACHUSETTS INSTITUTE OF TECHNOLOGY

August 2013
[SEPTEMBER 2013]

Author .....
Department of Mechanical Engineering
August 9, 2013

Certified by....: .....
Pedro M. Reis
Esther and Harold H. Edgerton Assistant Professor of Mechanical Engineering and Civl and Environmental Engineering
Thesis Supervisor

Accepted by .....
David E. Hardt
Ralph E. and Eloise F. Cross Professor of Mechanical Engineering
Chairman, Committee on Graduate Students

Localization of Deformation in Thin Shells under Indentation

by

Alice M. Nasto

Submitted to the Department of Mechanical Engineering
on August 9, 2013, in partial fulfillment of the
requirements for the degree of
Master of Science

Abstract

We perform a hybrid experimental and numerical study of the localization of deformation in thin spherical elastic shells under indentation. Past a critical indentation, the deformation of the shell ceases to be axisymmetric and sharp points of localized curvature form. In plates, these sharp points are known as d-cones. By way of analogy, regions of localization in shells are referred to as *s-cones*, for 'shell-cones'. We quantify how the formation and evolution of s-cones is affected by the indenter's curvature. Juxtaposing results from precision model experiments and Finite Element simulations enables the exploration of the frictional nature of the shell-indenter contact. The numerics also allow for a characterization of the relative properties of strain energy focusing, at the different loci of localization. The predictive power of the numerics is taken advantage of to further explore parameter space and perform numerical experiments that are not easily conducted physically. This combined experimental and computational approach allows us to gain invaluable physical insight towards rationalizing this geometrically nonlinear process.

Thesis Supervisor: Pedro M. Reis
Title: Esther and Harold H. Edgerton Assistant Professor of Mechanical Engineering and Civl and Environmental Engineering

Acknowledgments

Thanks to my supervisor Pedro Reis as well as my colleagues, Amin Adjari, Arnaud Lazarus, and Ashkan Vaziri, with whom I conducted this research in collaboration. I also acknowledge support from the NSF through Graduate Research Fellowship Program and from MIT through the Ascher H. Shapiro Graduate Fellowship.

Contents

Chapter 1

Introduction

1.1 Motivation

A thin shell is one whose thickness is small in comparison to other dimensions, such as the radius. Localization in thin shells is observed over a large range of lengthscales. At the microscale, colloidal capsules [1] can buckle under osmotic pressure (an image of these buckled capsules is shown in Fig. 1-1b). Other examples include bacteria [2], virus capsids [3, 4], and microcapsules [5] whose mechanical response can be measured, for instance, via Atomic Force Microscopy (AFM), where a probe with a sharp tip is used to scan an object at a resolution down to the nanoscale [6]. An example of an AFM image of an indented virus capsid at the nanoscale is shown in Fig. 1-1a. The curvature of the AFM tip relative to the curvature of the object that it indents is often non-negligible, especially as AFM is progressing towards measuring smaller objects, such as proteins and virus capsids at the nanoscale [6, 7, 8]. As such, the relationship between the mechanical response and the nature of the indenter-object contact is critical for understanding how the shape of the probe affects the measurement and characterization of small objects. [9].

At the macroscale, the study of thin shells is relevant to vehicles and aircraft, whose outer bodies are often made from curved thin sheets of metal. The appearance of localized deformation can occur during collisions that cause car and aircraft bodies to dent or crumple [10, 11, 12]. Examples of a car and a plane damaged by

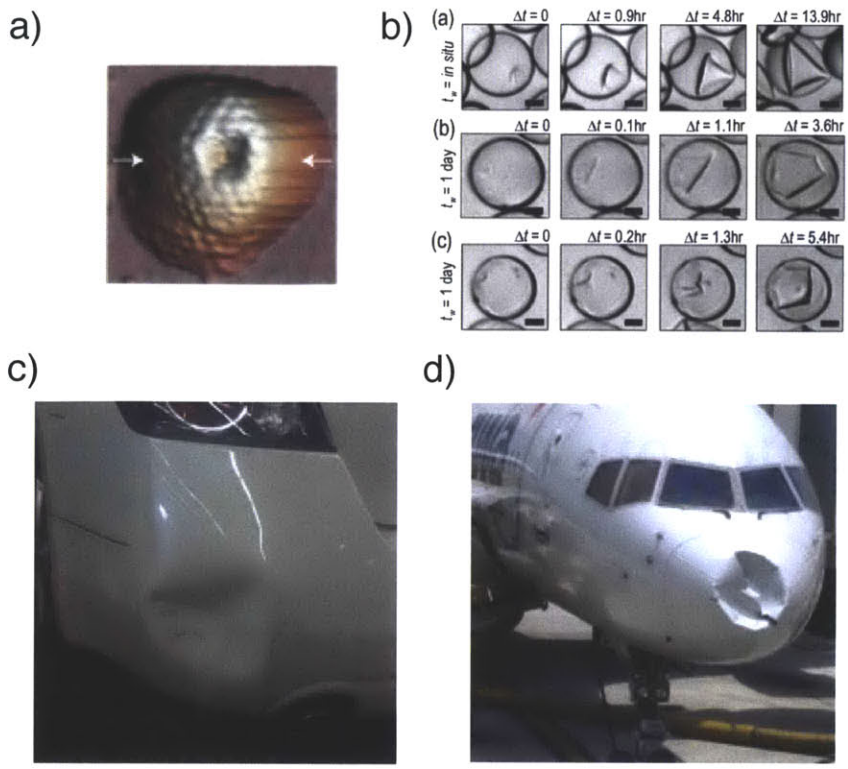

Figure 1-1: **Examples of localization across lengthscales.** a) AFM image of an HSV1 virus particle after nanoindentation (from Roos *et al.* [3]). b) Colloidal capsules at the microscale buckling under osmotic pressure (from Datta *et al.* [1]). c) Dented car bumper (photo courtesy of Pedro Reis). d) Airplane nose dented from a collision with a bird (from the NY Post).

collisions are shown in Figs. 1-1c,d. These initially smoothly curved surfaces now have dents with straight edges and sharp vertices along which the deformation is localized. In airplane and vehicle construction, engineers aim to design structures that are lightweight and thin, but also resistant to deformation and localization, which can cause permanent and costly damage. In these scenarios, understanding of the role of geometry and friction in shell-indenter contact and the mechanical response can inform how to design stronger structures and prevent localization.

1.2 Historical Perspective on Mechanics of Shells

Some of the earliest interest in the mechanics of shells in history is in the context of architectural domes. Poleni (1748) considered the structural stability of masonry domes for the construction of St. Peter's Basilica. He treated the dome as wedge shape arches and did not consider hoop forces, although they are crucial in many dome geometries [13].

In 1877, Lord Rayleigh [14] studied the vibrations of shells and wrote about how the deformation of thin elastic shells of thickness h involves both bending and stretching, with the elastic energy taking the form $\mathcal{E} = Ah(extension)^2 + Bh^3(bending)^2$. Further understanding of shell mechanics has since been developed in the twentieth century.

In the twentieth century, the elastic stability of thin shells has been of prime importance in airplane construction [15]. The axial compression of cylindrical shells and curved sheet panels has been treated extensively by Timoshenko in the early twentieth century [16]. For the application of modeling submarine hulls, von Mises studied cylindrical shells under axial and lateral pressure [17]. Buckling of spherical shells under uniform pressure was investigated by Zoelly [18], van der Neut [19], and Biezeno [20] in the early twentieth century. Biezeno posed the first solution based on non-linear equations for shells. Experiments on the buckling of thin shells revealed that the critical loads had been overestimated by classical theory [21, 22, 23]. This discrepancy between classical theory and experiments was explained by von Kármán and Tsien [24], who showed that by applying theory of large deflections, a stable equilibrium requiring smaller loads can be obtained. In the 1960's, experiments on the stability of clamped and simply-supported caps were carried out by Evan-Iwanowski [25] and Berke [26]. Reissner [27] derived the shallow shell equations for spherical shells, which is applicable to deformations near the apex of the shell. Ashwell [28] observed a region of inverted curvature (i.e. a dimple) whose size increases with load and proposed a solution based on approximate solutions for the inverted and outer regions. Singular perturbation methods, which provide a more

accurate description of the dimple, were later proposed by Koiter [29].

More specifically, we will now discuss past work on the loading of hemispherical caps through indentation at the pole, which is of particular relevance to the work we present here. The problem of a thin spherical shell deformed by a point load was considered by Landau and Lifshitz [30], and later solved by Pogorelov [31] in the 1980's, who derived the scaling laws for the radius of the circular fold that forms when the cap inverts (a schematic of this is shown in Fig. 1-2a). Pogorelov described two separate regimes with scaling laws. The first is the linear regime, where the displacement, e, is proportional to the force, F, for small forces. Including the thickness, h, and the radius, R, in this scaling, the force scales as $F \sim \frac{Eh^2}{R}e$ for the linear regime. Second is the regime of the inverted cap with a axisymmetric round ridge, in which the force scales as $F \sim \frac{Eh^{5/2}}{R}e^{1/2}$. Pogorelov also described a scaling argument for the elastic energy of the circular ridge, which scales as $\mathcal{E}_{ridge} = \frac{Eh^{5/2}e^{3/2}}{R}$.

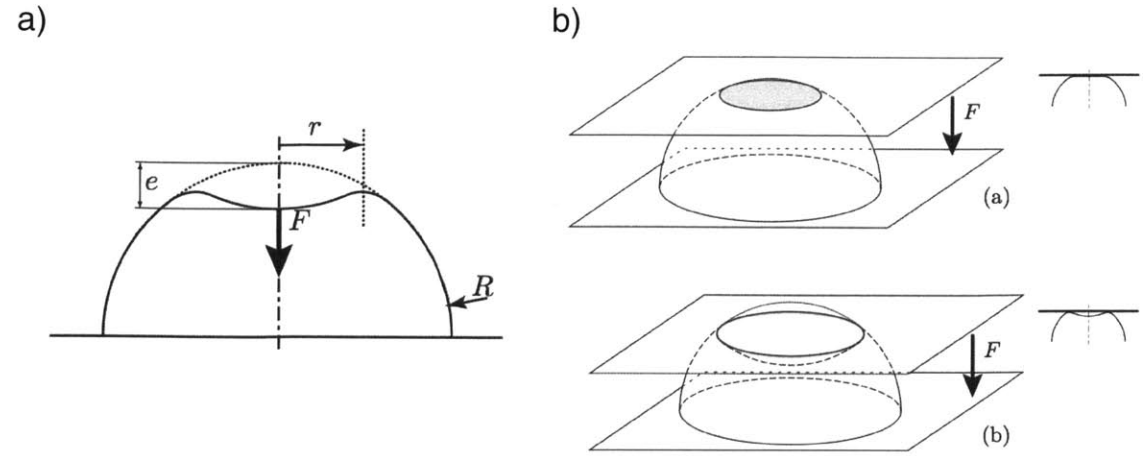

Figure 1-2: **Shells under point and plate indentation.** Schematics from Audoly and Pomeau [32]. a) Spherical shell under point indentation forming a circular ridge, as described by Pogorelov [31]. b) Spherical shell under plate indentation as described by Updike and Kalnins [33, 34]. For small forces, the shell makes a disc-like contact with the plate. For larger loads, the shell delaminates from the plate and forms an axisymmetric dimple.

The case of a spherical shell indented by a rigid flat surface was studied by Updike and Kalnins [33, 34] in the early 1970's, who provided analysis for disc-like contact for small forces, and circular contact for large forces, when the shell buckles and delaminates from the plane and forms an axisymmetric dimple (a schematic of these two configurations is shown in Fig. 1-2b). For the disc-like contact, two regions are specified and analyzed separately: the region of contact, and the outer free part of the shell. The authors showed that the contact pressure is concentrated near the edge of the contact region. The lower bound for energy of the disc scales as $\mathcal{E}_{disc} \gtrsim \frac{Ehe^3}{R}$. In the case of circular contact, the applied pressure is localized along a circle, and the elastic energy scaling is the same as for the Pogorelov ridge under point indentation.

1.3 Mechanics and Geometry of Shells

The mechanics of shells is inextricably connected to its geometry [16] and, for a shell with positive Gaussian curvature, bending and stretching are intrinsically coupled. Stretching is energetically costly compared to bending and the deformation of a shell is governed in large part by a need to minimize stretching, in favor of bending, to preserve the isometry of the surface. Isometric deformations are such that the distance along the surface between any two points is preserved, i.e. the surface does not stretch. In the linear regime (in which the load is linearly proportional to the displacement), there have been a number of attempts to rationalize the interplay between geometry and mechanics, ranging from the seminal work of Reissner [27] on spherical shells to the more recent study of geometry-induced rigidity in non-spherical pressurized shells [35].

Following an approach from Audoly and Pomeau [32], similar to that for Föppl-von Kármán equations for plates, where the elastic energy is the sum of the bending and stretching energy, the equilibrium equations for spherical shells can be derived, under the simplifying assumption of deformations near the apex where the size of the dimple is much smaller than the radius of the shell [32]. First, we start with the spherical reference shape, which is parametrically defined in cylindrical coordinates

(ρ, θ, z) by

$$\rho(s) = R\sin\frac{s}{R}, \quad z(s) = R\cos\frac{s}{R}, \tag{1.1}$$

where s is the arc length and R is the radius. In the neighborhood of the apex of the shell, $s << R$, one can use the assumptions,

$$\rho(s) \approx s, \quad \rho'(s) \approx 1, \quad z'(s) \approx -\frac{s}{R}, \tag{1.2}$$

which leads to what have been called by Reissner the *shallow shell* equations [27] . From following the kinematics and using the constitutive relations, the equilibrium equations we arrive at are,

$$\left(\frac{1}{s}\frac{d(sN_s(s))}{ds} - \frac{N_\theta(s)}{s}\right) + f_r(s) = 0, \tag{1.3}$$

$$\frac{1}{s}\frac{d}{ds}\left(sN_s(s)\left(-\frac{s}{R} + \phi(s)\right)\right) - \frac{D}{s}\frac{d}{ds}\left(\frac{d(s\phi'(s))}{ds} - \frac{\phi(s)}{s}\right) + f_z(s) = 0, \tag{1.4}$$

where $D = \dfrac{Eh^3}{12(1-\nu^2)}$ is the bending modulus (E is the Young's modulus, h is the thickness of the shell, and ν is Poisson's ratio), and $\phi(s) = -z'(s)v_r'(s) + \rho'(s)v_z'(s)$ is the first order rotation to the tangent to the generating curve (where v_r and v_z are the components of displacement in the r and z directions). The components of external force are $f_z(s)$ and $f_r(s)$ and the membrane stresses N_θ and N_s are the integrals over the thickness of the stress components $\sigma_{\theta\theta}$ and σ_{ss}, respectively.

The shell equations we have just described are valid only for the assumption of deformation near the apex and are not valid for large deformations where we can see non-axisymmetric buckling such that the surface develops sharp angular features. During the formation of sharp angular features, energy localizes at vertices and along straight edges, which, although locally costly, still minimizes stretching globally [36]. A general predictive framework for localization in shells under large deformations has not yet been developed.

1.4 Analogy to Localization in Plates

The scenario for large deformations in doubly-curved shells is similar to what is observed in plates and other developable surfaces (e.g. plates, conical, and cylindrical shells) under large deformations. When geometric constraints are placed on a plate, through compression or crumpling for example, energy localizes along *ridges* and vertices, known as *d-cones* for 'developable cones' [37, 32]. An example of this, a crumpled piece of foil, is shown in Fig. 1-3a, where we see the formation of these localized features in a polygonal network. This localization of deformation along small regions allows the rest of the surface to remain developable and minimizes stretching energy globally. These two localized structures, d-cones and ridges, have been well studied and characterized through experimental, numerical, and theoretical work [37, 32].

The Föppl-von Kármán equations for plates have been applied to ridge singularities, which were first analyzed using scaling laws by Lobkovsky *et al.* [40]. The geometry of the ridge (shown in Fig. 1-3b) is produced by creating a fold in the sheet (of length L and thickness h) which is applied to a rigid frame along its two edges at a prescribed dihedral angle $\pi - 2\alpha$. Using a scaling argument based on the bending and stretching energy along the fold, the energy of the fold is found to be of the order $\mathcal{E}_{fold} = Eh^{8/3}\alpha^{7/3}L^{1/3}$. Lobkovsky later analyzed this geometry through a boundary layer analysis [38] and this problem has been solved numerically [41, 32].

Experimentally, d-cones have been studied by forcing a thin sheet through a circular hoop using a sharp point indenter [42, 39] (shown in Fig. 1-3c). Other studies have looked at more complex geometries that comprise networks of several d-cones that evolve under loading [43, 44]. As for ridge singularities, theoretical understanding of d-cones has also been developed through the application of the Föppl-von Kármán equations and boundary layer methods to the geometry of the sheet pushed through a hoop to arrive at numerical solutions [45, 32]. Far from the tip of the cone, the elastic energy is dominated by the bending contribution. Numerical solutions have been found for the d-cone far from the tip. However, for the region close to the tip, a solution is still unsettled and even the size of the region is still up for debate [32].

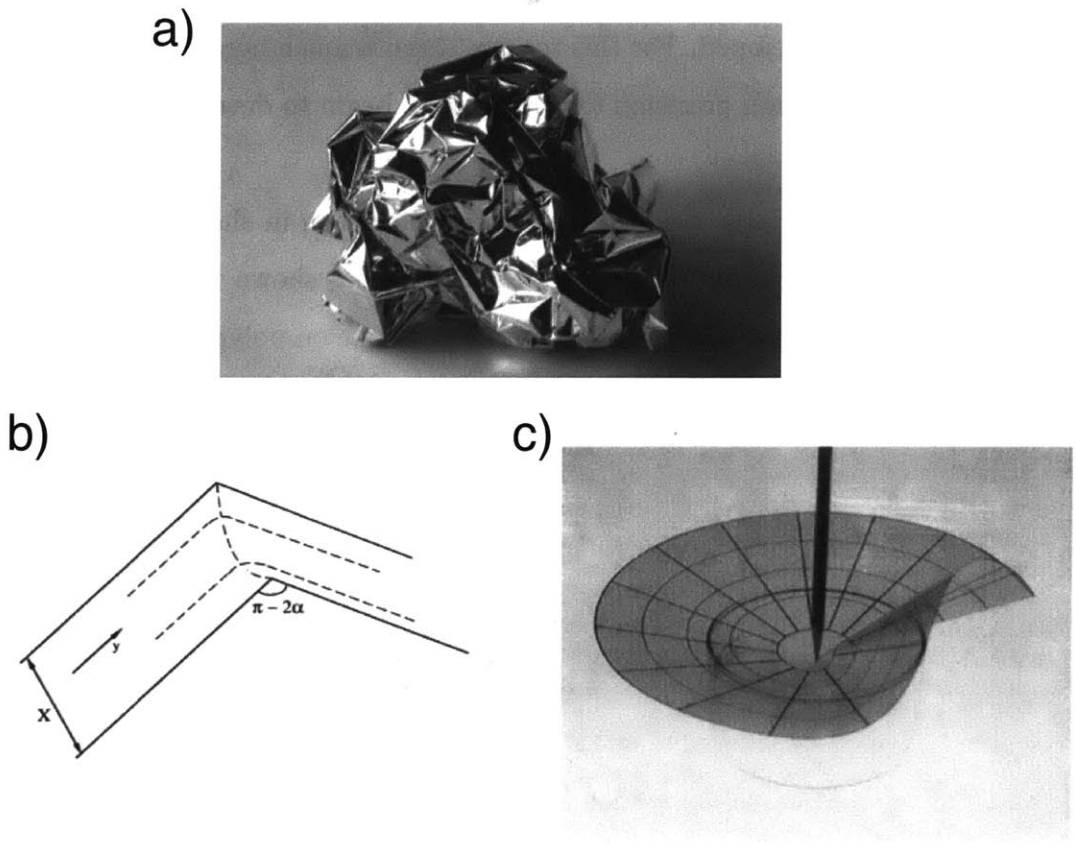

Figure 1-3: **Energy focusing in sheets.** a) Crumpled foil showing a network of polygons where energy localizes along vertices and straight lines (from Audoly and Pomeau [32]). b) Ridge singularity formed by folding a sheet through a dihedral angle $\pi - 2\alpha$ (from Lobkovsky [38]). c) A sheet pushed with a sharp point through a hoop, forming a d-cone (from Cerda and Mahadevan [39]).

Drawing an analogy with d-cones in plates and cylindrical shells [43], we designate the localized objects in doubly-curved shells as *s-cones*, short for 'shell cones'. The key distinction to emphasize is that doubly-curved shells are not developable.

1.5 Previous Studies on Localization in Shells

The formation of localized polygonal structures (i.e. s-cones) in shells occurs far beyond the initial buckling threshold in the post-buckling regime [32]. The previous work on shells discussed thus far correspond to deformations below the threshold for the formation of localized structures. Though the appearance of s-cones can be sup-

ported through scaling arguments [38, 46], a full theoretical groundwork for s-cones is far from being fully developed. For this reason, there is much need for an exploration of parameter space though precision experiments to begin to develop an understanding of s-cones.

Previous studies on large deformations and localization in shells have considered a variety of loading mechanisms. Experimental work has shown that colloidal particles that are depressurized through evaporation can take on polygonal conformations [47]. Other studies on depressurization of spherical shells primarily follow numerical and theoretical approaches to characterize a variety of buckled shapes, which include configurations with localized deformation [48, 49, 50].

For studies of shells that are deformed by indentation, the most common scenarios involve either point loading or plate loading. Vaziri and Mahadevan [36] conducted a numerical investigation of an elastic hemispherical shell under point indentation. For large indentation, they showed that the round ridge that forms loses its axisymetry and three sharp vertices along which the deformation is localized appears. Upon further indentation, there is a transition to a configuration with four vertices, and later a transition to five and six vertices. Vaziri [51] also studied plate indentation through a numerical study, and showed that five localized vertices form under plate indentation. Some experimental studies on localization have been conducted using ping pong balls, either through indenting single balls or by compressing packings of balls [52, 53]. The consideration of the effect of plasticity in the indentation of shells has been investigated in a few studies with numerical simulations and experiments on metal shells [54, 55, 56].

Previous studies on the indentation of shells focus on the two extremes of point load and plate load indentation. What is lacking is a systematic investigation of the effect of indenters of various curvatures on localization between the two limits of zero and infinite indenter curvature. To fill this need, we conduct precision model experiments where the various geometric and material properties and parameters can be accurately controlled, which is needed to explore this parameter space.

1.6 Outline of Thesis

In this thesis, we study indenters with intermediate curvatures are studied, filling the gap between point and plate indentation. We perform precision model experiments using hemispherical elastomeric shells and indenters with custom controlled geometries that we fabricate using rapid prototyping. The indenters have a range of radii of curvature, such that the ratio between the radius of the indenter, R_2, and that of the shell, R_1, defined as $\Gamma = R_2/R_1$ (shown schematically in Fig. 2-1d), lies in the full range $0 < \Gamma < \infty$, from point load to plate load, respectively. The mechanical response is quantified through indentation tests and the evolution of the deformation of the shell is captured with digital images using a camera located underneath the shell. In parallel, Finite Element Analysis (FEA) of the same scenario explored experimentally are performed.

The details of the materials, geometries, and methods involved in the experimental and numerical study are detailed in Chapter 2. In Chapter 3, we begin by investigating the case of point indentation in Section 3.1 through both experiments and FEA simulations and find excellent agreement between the two. Given the predictive power of our numerics, in Section 3.2, the simulations are then exploited to gain further insight into the characterization of localization of strain energy, a quantity that cannot be readily accessed experimentally. In Section 3.3, we systematically vary the shape of the indenter and observe that the indenter's shape affects both the number of s-cones that form as well as the indentation onset of localization. We investigate the geometry of shell-indenter contact in Section 3.4 and explore a purely geometric argument to rationalize the effect of the indenter shape and find important qualitative differences are observed between sharp indenters ($\Gamma < 1$) and blunt indenters ($\Gamma > 1$). In Section 3.5, we explore the effect of friction on the mechanical response and show that friction is necessary to include in the FEA model to agree with the experiments. The work described in the outline thus far has been published recently by the author with her colleagues [57].

Taking advantage of the predictive power of the numerics, we conduct an explo-

ration of parameter space through FEA simulations in Chapter 4. We demonstrate the prominence of geometry in the indentation of shells and show that localization in shells and the mechanical response is minimally dependent on self-weight (in Section 4.1) and independent of shell size (in Section 4.2). In Section 4.3, we quantify the maximum principal strains strains and find that they remain small despite large macroscopic deformations. Given that the strains remain small, in Section 4.4, we demonstrate the applicability of our results beyond hyperelastic elastomeric materials to linear elastic materials, since material non-linearities do not play a role. In Section 4.5, we show that the ratio of the thickness of the shell to the radius, t/R_1, has a significant effect on the onset and evolution of s-cones, as well as the extent of localization at the s-cones. Motivated by our discovery of the importance of friction in the experimental system, in Section 4.6, we perform a systematic investigation of the effect of friction and demonstrate that friction acts to suppress localization and strengthen shells.

Chapter 2

Physical and Numerical Experiments

In this chapter we describe the methods and parameters used for the physical experiments and the numerical simulations, both of which we perform in tandem. Rapid prototyping techniques were employed to fabricate shells and indenters used in the physical experiments, which were then mechanically tested for precision quantification. The numerical simulations were carried out using the finite element method.

2.1 Geometry and Configuration of the Tests

A thin hemispherical shell clamped at the edge of its equator is indented quasi-statically (i.e. slowly enough such that dynamic effects are negligible) at the pole along its vertical axis. The curvature of the indenter relative to the shell is varied. This scenario is carried out through both physical and numerical experiments.

For the experimental and numerical studies conducted in Chapter 3 and the study on the effect of weight in Chapter 4, the shell has a radius of radius $R_1 = 25$ mm and thickness $t = 0.3 \pm 0.01$ mm. Note that $t/R_1 = 0.012$, which ensures that our structures are in the thin shell limit. For the numerical studies conducted in Chapter 4 (with the exception of the study on the effect of weight), the shell has a radius of $R_1 = 1$ m and a thickness of $t = 1$ cm ($t/R_1 = 0.01$). The reason for this change is

that in Chapter 4 we show that the mechanical response is scalable with the radius, as long as t/R_1 remains the same and this choice presented advantages in the numerical implementation.

The indenters have a range of radii of curvature, such that the ratio between the radius of the indenter, R_2, and that of the shell, R_1, defined as $\Gamma = R_2/R_1$ (Fig. 2-1d), lies in the range $0 < \Gamma < \infty$, from point load to plate load, respectively (examples of these indenters are shown in Fig. 2-1e).

2.2 Fabrication of the Shell

Both the shells and the indenters are fabricated using rapid prototyping techniques. Vinylpolysiloxane (a silicone based elastomer with the product name Zhermack Elite Double 32) was used to make the shells. VPS has a density of $\rho = 1.2\ g/cm^3$, a shear modulus of $G_0 = 454.6\ kPa$, and a Poisson's ratio of $\nu = 0.5$. A Neo-Hookean model, a hyperelastic constitutive description that is appropriate for elastomeric materials that are non-linearly elastic, was used to describe the material [58]. The Neo-Hookean strain energy potential for VPS is $\psi = C_{10}(\bar{I}_1 - 3) + \frac{1}{D_1}(J-1)^2$, with the coefficients $C_{10} = 227300\ Pa$, and $D_1 = 2.36 \times 10^{-8}\ Pa^{-1}$ determined directly from experiments (described in detail below). The coefficients are related to the shear modulus G_0 and the bulk modulus K, with $C_{10} = G_0/2$ and $D_1 = 2/K$, respectively. The determinant of the deformation gradient is $J = det(\boldsymbol{F})$ and $\bar{I}_1 = J^{-2/3}I_1$ is the first invariant of the deviatoric part of the left Cauchy-Green deformation tensor [58].

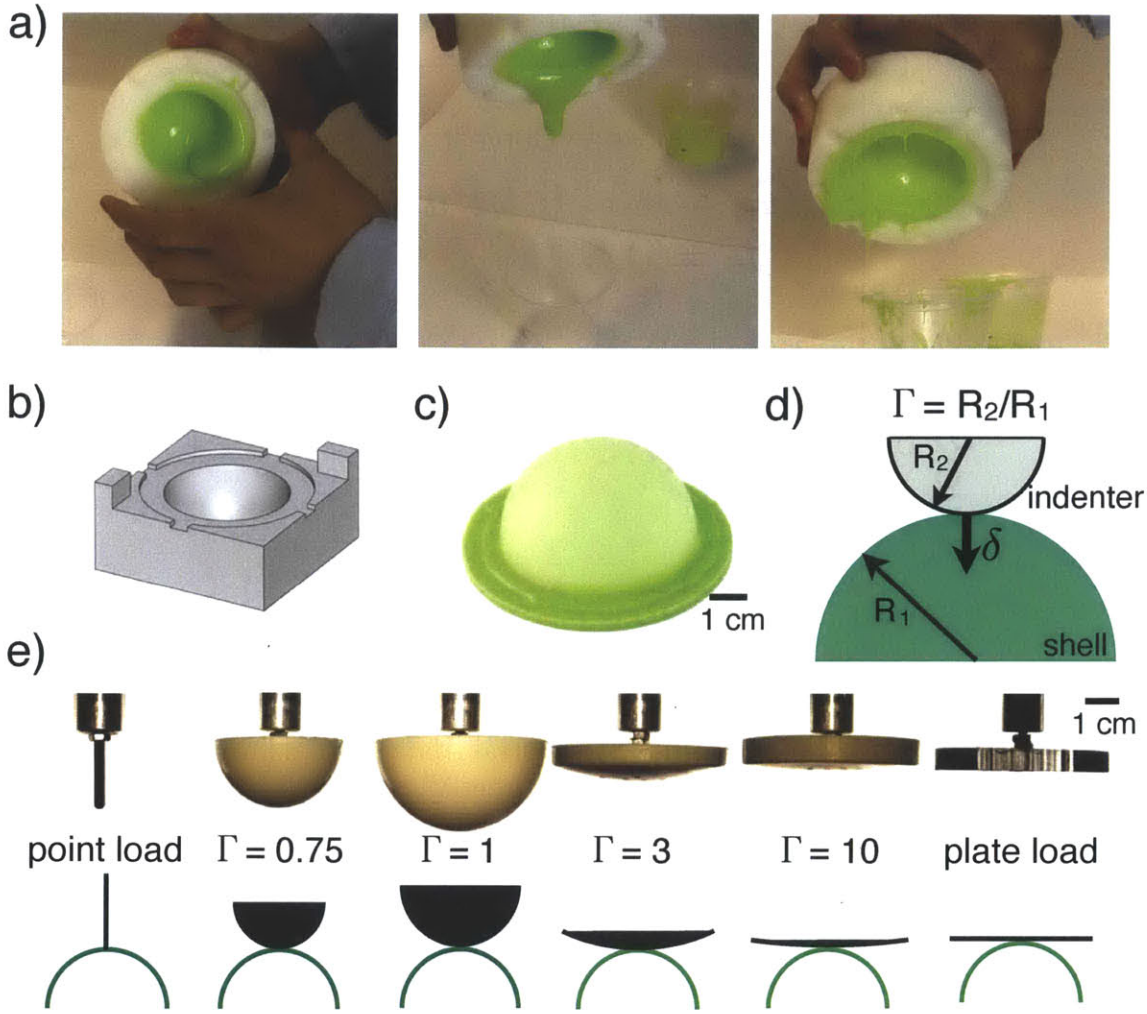

Figure 2-1: **Shell and indenter fabrication.** a) Coating technique used to fabricate thin and uniform hemispherical shells. b) CAD model of indenter and shell molds. c) Hemispherical elastomeric shell created by the coating technique. d) Schematic of shell, with radius R_1 and indenter, with radius R_2 e) Series of indenters ranging from $\Gamma = R_2/R_1 = 0$ (point load) to $\Gamma = \infty$ (plate load).

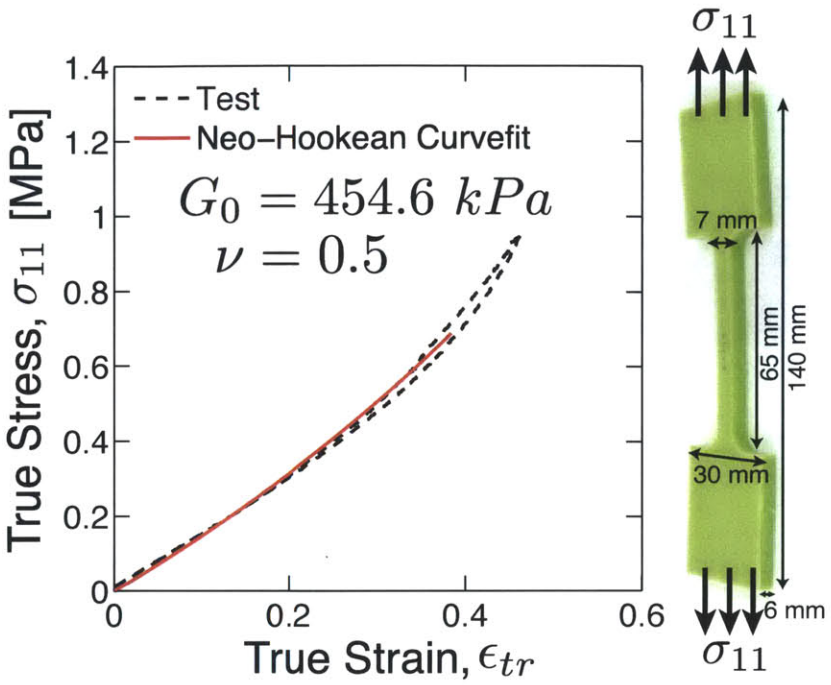

Figure 2-2: **Neo-Hookean curve-fit.** Stress-strain data (dotted line) from a uniaxial tension test on a dogbone-shaped sample cast from VPS. The Neo-Hookean model is fit from this data (plotted in red).

The coefficients C_0 and D_1 of the Neo-Hookean model were determined by performing a curve fit on the data from a uniaxial tension test on a dogbone-shaped specimen made out of VPS (dimensions of the specimen are shown in Fig. 2-2). The stretch-stress expression used for the incompressible Neo-Hookean uniaxial tension curve fit is $\sigma_{11} = 2G_0(\lambda^2 - \frac{1}{\lambda})$ where σ_{11} is the true stress and λ is the stretch, both in the direction that the sample is pulled in tension. To find the bulk modulus and the Young's modulus, the Poisson's ratio is set to $\nu = 0.4975$ so that the material is nearly incompressible (if the material were modeled as perfectly compressible with $\nu = 0.5$, the bulk modulus is infinite and the coefficient D_1 would be zero). The Young's modulus and bulk modulus are related to the shear modulus and Poisson's ratio such that $E = 2G_0(1 + \nu)$ and $K = \dfrac{E}{3(1 - 2\nu)}$. In Fig. 2-2, the true stress is plotted as a function of the true strain (as a black dotted line) for the VPS specimen under uniaxial tension. The red curve corresponds to the stress-strain curve obtained from using coefficients from a Neo-Hookean model that fit the experimental test data.

Two different methods for fabricating shells were explored. Ultimately, the second method for shell fabrication was chosen. The first method involved casting shells using a 3D printed two-part mold. Starting with a CAD model, a mold is designed for a shell with a specified target radius and thickness. The thickness is tuned by the relative sizes of the two mold parts. The shell is then cast using the VPS silicone polymer. The resulting shell has a thickness $t = 0.5$ mm with up to 60% variation in thickness. This variation in the thickness is due to limitations of the resolution of the 3D printer (Dimension uPrint), which imprints a texture on the printed mold parts with a characteristic length scale of $\sim 178\ \mu m$, which is the diameter of the ABS plastic filament.

The second method for fabricating shells involves a coating technique pictured in snapshots from the fabrication process in Fig. 2-1a. A mold made of polyacetal was machined through CNC milling, which results in a smoother surface finish in comparison with the 3D printed mold above. The silicone polymer was poured into the mold and then rotated so that the polymer wetted its entire surface. The excess was then poured out and the mold was left upside-down to allow the excess to drain while the polymer cured. The resulting shells have a thickness of $t = 0.28 \pm 0.027$ mm, which is set by a balance between the viscosity and surface tension of the polymer and curing rate, although the process is not understood in detail. In a scenario similar to Landau-Levich dip coating for fibers and plates [59], this fabrication method results in shells with small variations on their thickness ($\sim 9.7\%$). Compared to the casting method described above, this method creates shells that are approximately 40% thinner and 5 times more uniform.

To compare these two fabrication methods, we consider the mechanical response of the two different shells under point indentation, as measured through load-displacement curves plotted in Fig. 2-3 a) (details of mechanical testing are given in Section 2.4). For shells fabricated using the first method, the load-displacement curve for the casted shell has many local minima and maximum, which appear because of the variation in thickness. This variation is demonstrated by the profile of the shell, which is obtained by scanning the cross-section of the shells after they have been cut in half (Fig. 2-3

b). In contrast, the mechanical response of the coated shell (the second fabrication method) increases monotonically and is smoother since the thickness profile is untextured and more uniform (Fig. 2-3 c). For thin shells in the nonlinear regime (past a small indentation where the load response is nonlinear), the mechanical response is considerably imperfection sensitive. It is clear that the second method for shell fabrication is therefore preferred for studying localization, which occurs in the nonlinear regime.

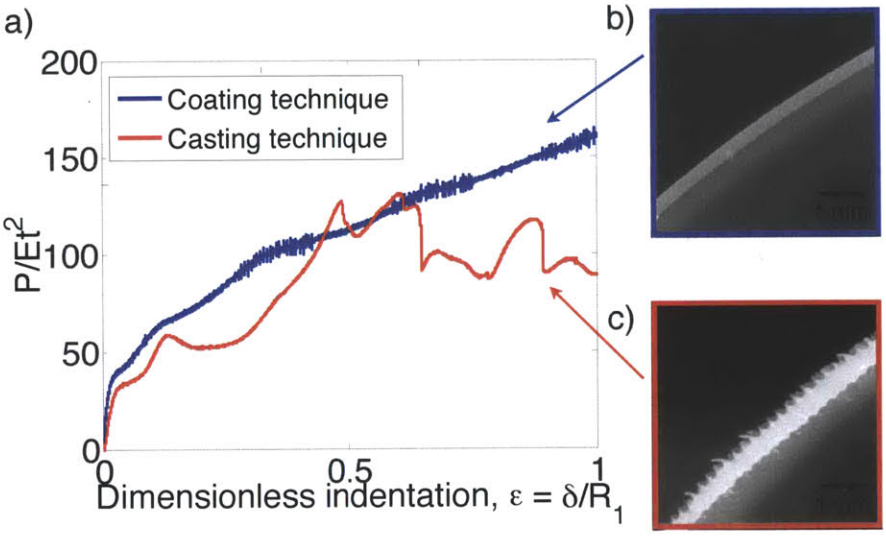

Figure 2-3: **Comparing shell fabrication techniques.** a) Non-dimensional force-indentation curves for the shells fabricated with the coating technique (in blue) and the casting technique (in red). The dimensionless indentation is defined as $\epsilon = \delta/R_1$ where δ is the depth of indentation and R_1 is the shell radius. b) Scanned profile of a shell fabricated from the coating technique (Method 1). c) Scanned profile of a shell fabricated from the casting technique (Method 2).

2.3 Fabrication of the Indenters

Twelve indenters were designed with a variety of radii of curvature so that the ratio of the radius of the indenter and the radius of the shell, $\Gamma = R_2/R_1$ had the following values: $\Gamma = 0$ (point load), $0.5, 0.75, 0.8725, 1, 1.5, 2, 3, 5, 7, 10$, and ∞ (plate load) (a schematic of the indenters is shown in Fig. 2-1e). Indenters with Γ ranging from 0.5 to 10 were cast out of a hard polyurethane using a mold made of polyacetal that

was machined using CNC milling. The indenter for point load was a steel screw with a hemispherical cap (1.5 mm radius). The indenter for plate load was laser cut from a sheet of acrylic. All indenters can be considered rigid relative to the elastomeric shells since the polyurethane used to cast the indenters has a Young's modulus $E = 147\ MPa$, whereas the VPS used to cast the shells has a Young's modulus $E = 1.36\ MPa$.

2.4 Mechanical Testing and Imaging

A photo of the mechanical testing and digital imaging setup is shown in Fig. 2-4. Shells are indented at their pole using the fabricated indenters at the constant speed of 5 mm/min, such that the strain rate defined with the shell's radius is $3.3 \times 10^{-3} s^{-1}$. The compressive force, P, resulting from the indentation by the imposed displacement, δ, is recorded using the load cell of an Instron 5943 machine with a resolution of $\pm 100 \mu$N. The evolution of the deformation of the shell is recorded with digital images that are captured from underneath the shells at a rate of one frame per 0.5 mm of indentation. The light source is a fluorescent light ring placed around the lens of the camera to provide homogeneous lighting. This lighting arrangement is optimal for visualizing localization since a sharp white reflection lines can be seen on the surface of the shell along the regions where the shell inverts and forms a ridge on which localized structures form (examples of these images can be seen in Fig. 2-4 b).

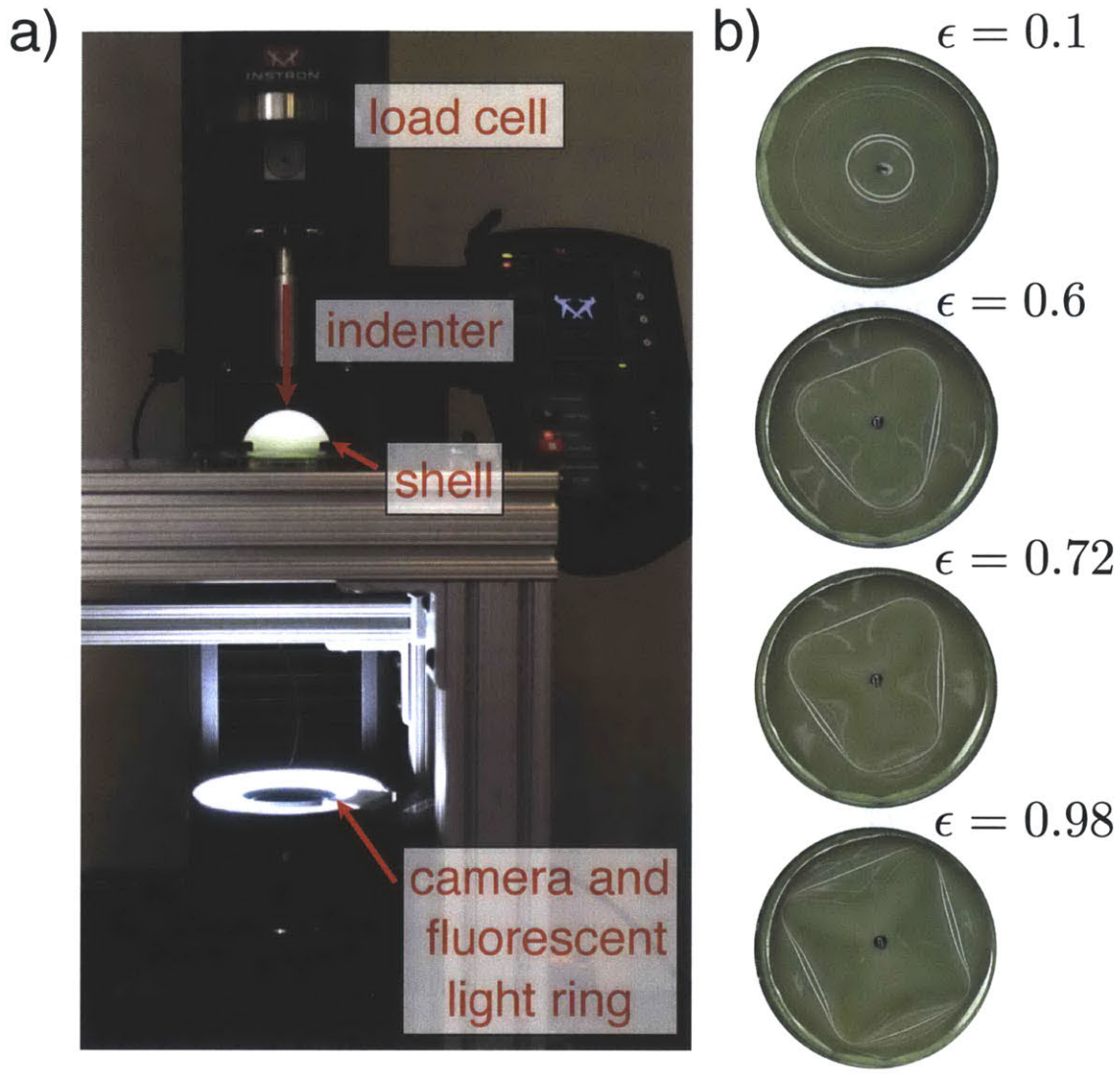

Figure 2-4: **Mechanical testing and imaging arrangement.** a) A photo of the mechanical testing setup using an Instron materials testing machine. The load cell applies a load to the shell through an indenter, which indents the shell at the pole. Underneath the shell, a camera and a fluorescent light ring are used to capture digital images as the shell is indented. b) Images from underneath the shell as it evolves under point indentation.

2.5 Friction Tests

The friction from the contact between the shell and the indenter was estimated through friction tests. A block (with dimensions 30 mm by 45 mm by 60 mm) of Vinylpolysiloxane (the shell material) with a force sensor attached was pulled horizontally along a surface made of polyeurethane (the indenter material). The coefficient of friction, measured through these tests was $\mu = 1.46 \pm 0.53$, the average from ten experiments of the ratio of the force required to pull the block to the weight of the block.

2.6 Numerical Simulations

Numerical simulations were performed using the commercial finite element package ABAQUS/CAE (SIMULIA, Providence, RI). The hemispherical shell was modeled with a clamped boundary condition on the free edge. The indenters were modeled as analytical rigid shells with a displacement-control boundary condition. For the material properties (except for the tests in Chapter 4 using a linear elastic model for a material model comparison), we used an isotropic hyperelastic model using the material parameters measured independently in the experiments. Four-node thin shell elements with reduced integration (element type S4R) were used in all simulations. S4R elements are general purpose shell elements that use Kirchoff shell theory in the thin shell limit. A mesh sensitivity study was carried out to ensure that the results are minimally sensitive to the element size. The free mesh scheme available in ABAQUS was used and no initial geometric or material imperfection was included in the computational model. To capture the local instabilities in the structure, we used a stabilizing mechanism (available in ABAQUS/Standard solver) based on the automatic addition of volume-proportional damping, which was decreased systematically to ensure that the response was insensitive to this change. To model friction, a penalty formulation was used with the appropriate coefficient.

Chapter 3

The Role of the Indenter's Shape in Localization

In this chapter we conduct a combined series of experimental and numerical studies for the same material and geometric properties. By aiming to numerically capture the phenomena observed in the experimental study, we seek to gain insight towards understanding the essential physical ingredients involved in the indentation of our doubly-curved shells. In this chapter, we start by considering the case of point indentation. Under point indentation, we investigate the formation and evolution of s-cones and use numerics to understand the localization of energy across the various features. Then, we proceed by studying the effect of changing the shape of the indenter. We compare several quantities across indenter shapes, such as number of s-cones, critical indentation for s-cone formation, and ridge-height as a function of indentation. We investigate the role of geometry in the shell-indenter contact and friction, which we found to have a significant effect on the mechanical response.

3.1 Formation and Evolution of S-cones under Point Indentation

We begin by considering the case of point indentation. A thin hemispherical shell is clamped at its equator. A point load is then applied to the shell's pole along its axis and the indentation is performed quasi-statically at 5 mm/min (see Chapter 2 for more details). This same scenario is implemented and studied both experimentally and through FEA simulations. In the experiments, the evolution of the deformation upon indentation is captured through digital imaging, as shown in the sequence of photographs in Fig. 3-1a). The white lines in the photographs, which aid identifying the loci of localization, correspond to light reflections from the ridge-like regions, where the shell inverts. The FEA simulations provides additional means to quantify the localization process, for example by having access to the energy density as indicated by the color map in Fig. 3-1b). Localized structures are associated with sharp local increases in energy density.

In Fig. 3-1a,b) we present a sequence of representative snapshots of the shell at different stages of indentation, for the experiments and the FEA simulations, respectively, at the same values of indentation. We recall that the dimensionless indentation is defined as $\epsilon = \delta/R_1$, where δ is the indentation displacement and R_1 is the radius of the shell. Excellent qualitative and quantitative agreement is found between experiments and FEA simulations.

At small values of ϵ (e.g. $0.02 < \epsilon < 0.29$), the cap of the shell inverts inwards,

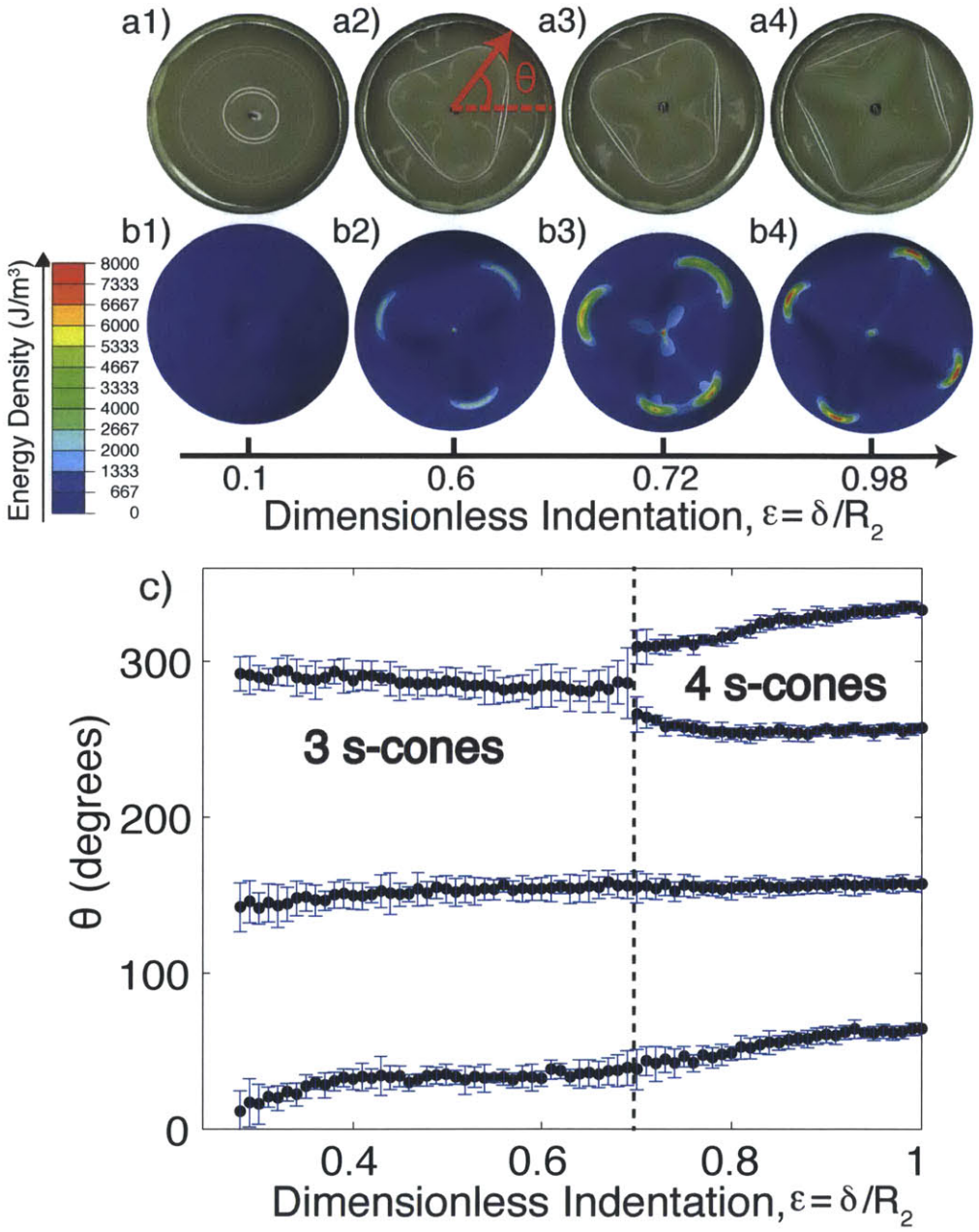

Figure 3-1: **Point indentation.** a) Experimental snapshots (captured from underneath the shell) of the evolution of the pattern of localization for an elastomeric shell under point indentation at the pole. The white reflection corresponds to the location at which the shell inverts. b) Snapshots from FEA simulations of an elastomeric shell under point indentation at the pole. c) Angular position of s-cones vs. indentation obtained from experimental images; θ is defined as in the red schematic drawn in a2.

forming an axisymmetric circular ridge, known as Pogorelov ridge [31], along which the shell stretches (Fig. 3-1a1,b1). Due to the high energetic cost associated with stretching, past a critical value of indentation, the round ridge loses its axisymmetry and strain focuses at three conical-like vertices (around $\epsilon = 0.295$), the *s-cones*, which help reducing the stretching globally (Fig. 3-1a2,b2) [51]. Once these three s-cones form, the inverted portion of the shell develops a tetrahedral shape. One vertex of the tetrahedron is located at the point where the indenter makes contact with the shell. The outer three vertices are located along a path on the surface where the shell inverts. These three s-cones are connected by straight segments, which we designate as *ridges*, acting as folds between the mostly undeformed outer shell and the inner inverted region. Inside the inverted tetrahedral region, additional folds form, which we refer to as *gullies*, that connect each of the s-cones to the point of indentation.

As the shell is indented further, the s-cones travel along the shell's surface and eventually new s-cones form (around $\epsilon = 0.69$). It is interesting to note that the birth of additional s-cones appears by division of an existing s-cone (Fig. 3-1a3,b3), rather than through nucleation at a previously smooth region of the shell. Further indentation past the splitting event results in four well defined s-cones (Fig. 3-1 a4, b4).

To further quantify the process of birth and growth of s-cones, digital image processing is performed on the experimental frames to track the angular position of each of the s-cones (projected on a plane perpendicular to the vertical axis of indentation). The schematic definition of the s-cone's angular position, θ, is presented in Fig. 3-1a2). As the shell is indented, the evolution of the s-cones' angular position illustrates the splitting mechanism by which new s-cones form; at $\epsilon \sim 0.7$, the forth new s-cone emerges through the branching of one of the older three. Outside the splitting region, at a higher indentation, the s-cones become more equally spaced in their angular positions θ.

The mechanical response of the shell is quantified with a load-indentation curve, as shown in Fig. 3-2, where we plot the load for a shell that is indented with a point load. For small indentation ($\epsilon < 0.02$), there is a linear regime where the load is

linearly proportional to the indentation. The load increases monotonically as the shell is indented. These findings are in contrast with some past numerical and analytical studies that predicted drops in the load-displacement curves when s-cones form, corresponding to reduction in apparent stiffness of the shell as an asymmetric buckling pattern occurs [36, 60, 61]. The monotonic increase in the load suggests that the formation of s-cones occurs through a continuous deformation, and not via snap-buckling, which would be accompanied by a drop in stiffness. We have not been able to rationalize the discrepancy between our experiment and previous numerical studies but hope that our results will motivate further developments.

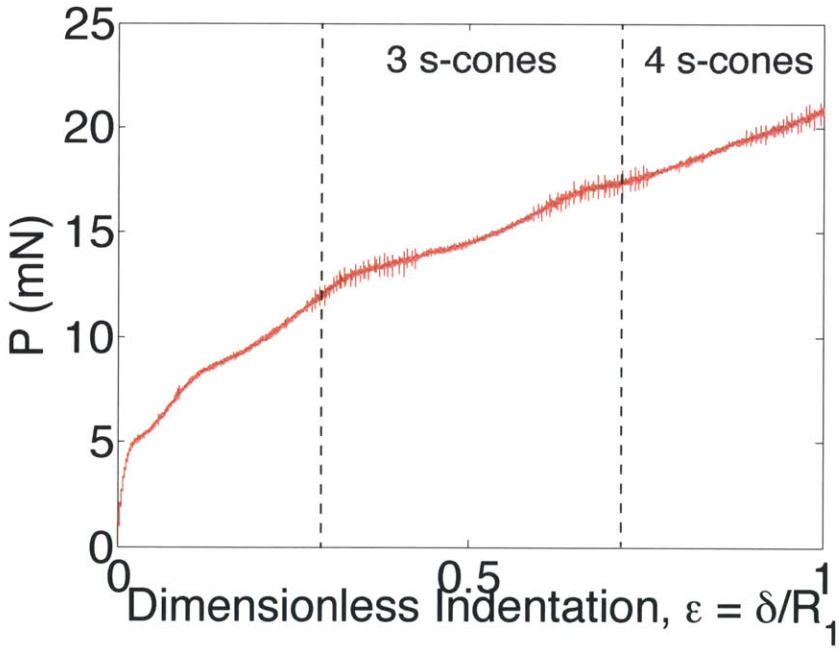

Figure 3-2: **Load under point Indentation.** Mechanical response of shell under point indentation is captured through experimental measurement of load as the shell is indented. Vertical dashed lines represent critical indentations at which 3 and 4 s-cones form.

3.2 Localization of Energy for Point Indentation

We further characterize the various localized structures identified above for point load, using quantities extracted from the FEA that are not available experimentally. In this section, we explore the power of the FEA simulations in predictively reproducing the experimental results. In particular, a quantitative comparison is made for the strain energy density $\mathcal{E}$, the energy stored in a body due to deformation per unit volume, between the *s-cones*, *ridges*, and *gullies*. We analyze the specific example of indentation to $\delta = 15mm$ (ϵ=0.6). The paths along the shell's surface that we shall use in our discussion are schematically drawn on top of the FEA snapshots shown in Fig. 3-3a,b).

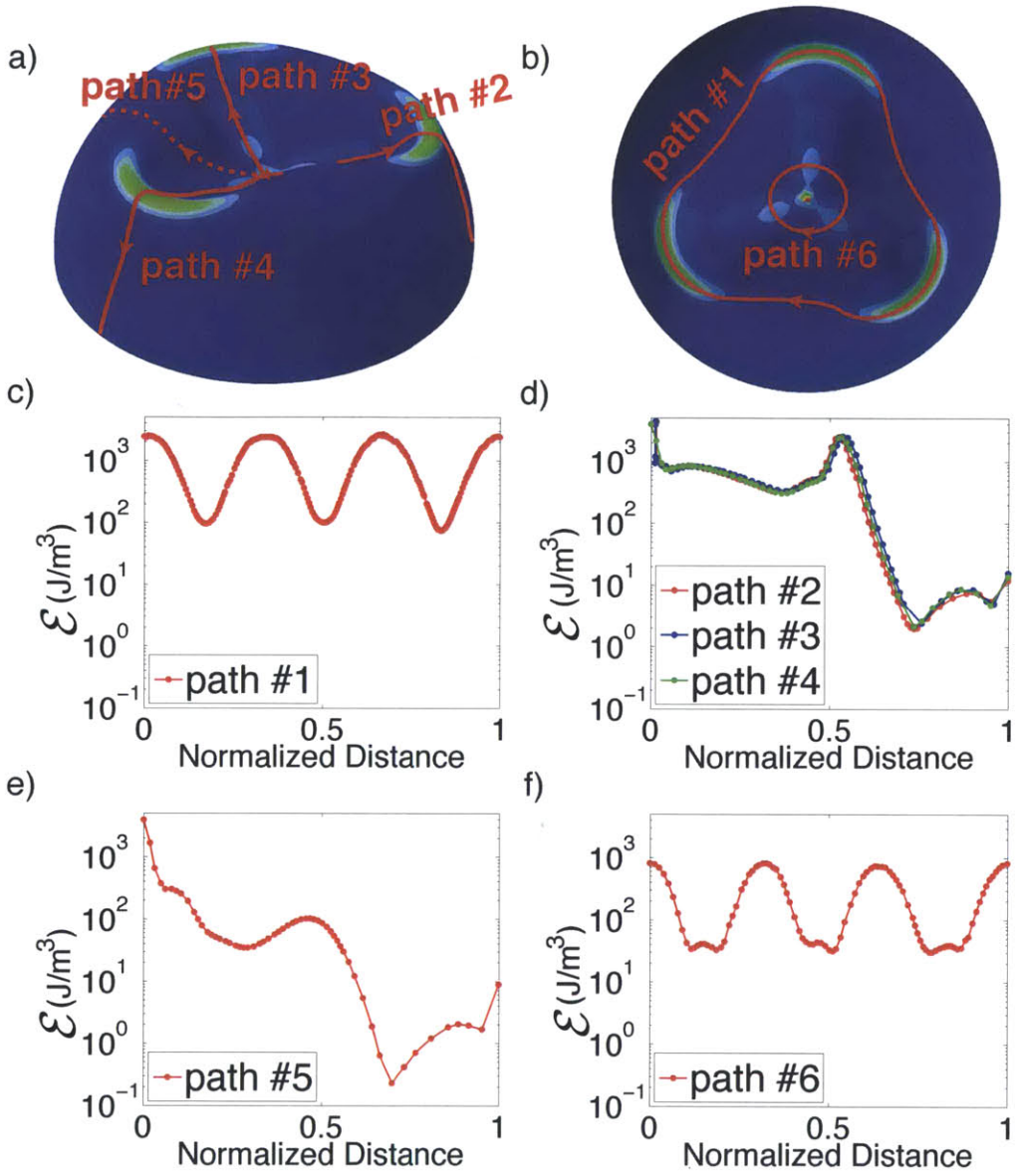

Figure 3-3: **Energy localization.** a,b) Snapshots from a finite element simulation of a shell indented with a point load. b) Top view. c) Energy density $\mathcal{E}$ along Path #1, which traces over the three s-cones and the three ridges that connect them. d) Energy density along Paths #2, #3, and #4 start from the pole of the shell, trace along one of the gullies and one of the s-cones, and end at the base of the shell. e) Energy density along Path #5, which starts from the pole of the shell, climbs between the s-cones and ends at the base of the shell. f) Energy density along Path #6, which intersects the three gullies.

In Fig. 3-3c, the energy density is traced along Path #1, which is a closed contour that traverses over the range of the three s-cones and the ridges that connect them. The energy density is highest at the s-cones and is minimum at the ridge's midpoint, half way between adjacent s-cones. The energy density level in the neighborhood of the s-cones is 25 times higher than along the ridges, which is significant of localization.

Paths #2, #3, and #4 define meridians; they start from the pole of the shell, pass along a gully, over one of the s-cones, and end at the shell's equator, with each of the paths passing over each of the three s-cones. In Fig. 3-3d), the energy density is plotted along these paths. The maximum of energy occurs at the pole where the indenter contacts the shell. Moving away from the pole, the energy density drops along the gullies, then sharply increases at the s-cones, before rapidly decaying by four orders of magnitude towards zero at the clamped equator of the shell. The energy density curves corresponding to these three paths are superposed, highlighting the symmetry of the process.

In Fig. 3-3e), the energy density is plotted along Path #5, which starts at the pole, traces along one of the faces of the tetrahedron, crosses over the ridge's mid point, and ends at the shell's clamped equator. As stated previously, energy is localized most intensely at the pole where the shell is indented. The strain energy along the face of the tetrahedron is small (1% compared to the energy localized at the s-cones). While climbing and traversing over the ridge, there is a small increase in strain energy, indicating that there is some focusing of strain energy at the ridge (4% compared to the energy localized at the s-cones). The energy then decays towards zero at the shell's equator, consistently with the clamping boundary conditions there.

In Fig. 3-3f), energy density is traced along Path #6, which is a circular contour near the shell's pole and crosses over the gullies and faces of the tetrahedron. Along this path, the energy is maximum at the gullies.

In summary for point indentation we find that energy is most strongly localized at the s-cones. Energy is localized to less of an extent along gullies and ridges, with energy being ten times more focused along gullies in comparison to ridges.

3.3 Varying the Shape of the Indenter

Having described the behavior observed for point indentation, we now consider the effect of changing the shape of the indenter on the localization process, in both experiments and FEA simulations. The ratio of shell and indenter radii is varied from $\Gamma = 0$ (for point load) to $\Gamma = \infty$ (for plate load), and we consider twelve indenters between these extreme values. In the experiments, rapid prototyping was employed to design and custom fabricate indenters (rigid with respect to the shells) with the range of radii of curvature shown in Fig. 2-1e). More information on how the indenters are fabricated was given in Chapter 2.

In Fig. 3-4, we show a series of representative experimental and FEA snapshots of the shells, for increasing values of the ratio of shell-to-indenter radii, Γ. In the experimental images, s-cones are identified by sharp corners in the ridge, as imaged by the white reflection line, and in the FEA simulations they are identified by small regions with a sharp increase in energy density. Localization occurs and s-cones form for all of the indenters, except for $\Gamma = 1, 1.5$ and 2. In the neighborhood of $\Gamma = 1$, the indenter has a curvature close to that of the shell. As a result, upon indentation their two surfaces remain in complete contact, preventing the formation of s-cones, which would otherwise require delamination from the indenter.

We refer to this neighborhood of $1 \lesssim \Gamma \lesssim 2$ as the "*localization band gap*", since the formation of s-cones is forbidden for these geometries. The lower bound for the localization band gap is $0.8725 < \Gamma < 1$ (uncertainty of $\sim 3\%$, based on the fact that simulations and experiments were not conducted within the given range) and the upper bound lies in $2 < \Gamma < 2.5$ (uncertainty of $\sim 11\%$). This band sets two regions with qualitatively different responses; sharp indenter for $\Gamma \lesssim 1$ and blunt indenters for $\Gamma \gtrsim 2$.

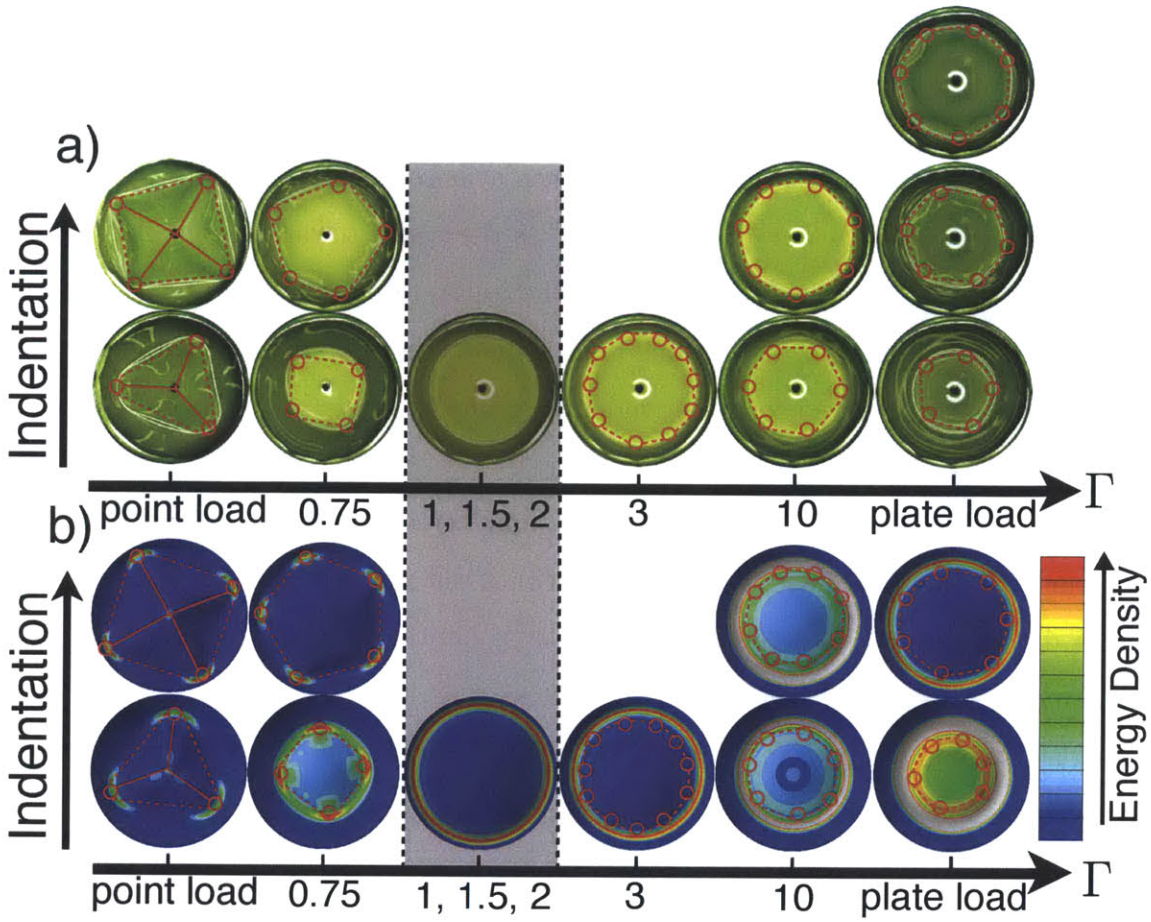

Figure 3-4: **Varying the shape of the indenters.** a) Snapshots from experiments with elastomeric shells indented at the pole for a variety of indenters, ranging from point load ($\Gamma = 0$) to plate load ($\Gamma = \infty$). b) The same scenario with the same snapshots in FEA simulations. The color map corresponds to strain energy density. The color and energy scale correspondence is adjusted for each of the images to aid in highlighting localization. Red circles indicate location of s-cones. Dashed red lines are drawn over ridges that connect s-cones along where the shell is inverted. Solid red lines are drawn over gullies that connect s-cones to the pole of the shell (only present for point load). No localization (indicated by grey area) occurs for indenters with $\Gamma = 1, 1.5$, or 2.

Concentrating on the experiments for sharp indenters, the number of s-cones at onset is a minimum ($n = 3$) for point load ($\Gamma = 0$) and it increases with increasing Γ, with the maximum number at onset forming just outside the localization band gap region. For blunt indenters, $n = 5$ s-cones form at onset for plate load ($\Gamma = \infty$), and increasingly more s-cones are observed as Γ is decreased towards $\Gamma \sim 2$. For the case of point load above, we saw that past the initial formation of 3 s-cones, a forth can emerge by splitting of a previous one. This mode of transition in the number of s-cones is also observed for other indenter geometries: $n = 4 \rightarrow 5$ for $\Gamma = 0.75$, $n = 6 \rightarrow 7$ for $\Gamma = 10$ and $n = 5 \rightarrow 6 \rightarrow 7$ for $\Gamma = \infty$ (plate load).

The FEA simulations show qualitative good agreement with this experimental scenario with differences in the number of s-cones varying at most by $n = 1$, possibly due to differences in the details of imperfections between experiments (defects) and FEA (meshing), or a consequence of the fact that multiple states may coexist (as is common in nonlinear systems but are difficult to capture through FEA). Moreover, FEA simulations also exhibit a localization band gap region for $1 \lesssim \Gamma \lesssim 2$ as well as the same qualitatively different responses for sharp indenters versus blunt indenters.

We have just seen that the geometry of the indenter strongly affects the morphology and number of s-cones at onset. We now quantify how the indenter's geometry also sets the critical indentation, δ_c, at the onset of localization, i.e. the δ at which the first set of s-cones forms. In Fig. 3-5, we plot the critical indentation as a function of Γ. As Γ approaches the band gap region in the neighborhood of $\Gamma = 1$, from either above or from below, the onset of localization is significantly delayed. The critical indentation exhibits a divergence-like behavior around the band gap region, and the critical indentation is maximum on either side. The critical indentation decreases as $\Gamma \rightarrow 0$ or $\Gamma \rightarrow \infty$ (with the exception of the decrease in δ_c between point load and $\Gamma = 0.5$, which disrupts the otherwise monotonic behavior to the left of the localization band gap). Excellent quantitative agreement is again found between experiments and simulations.

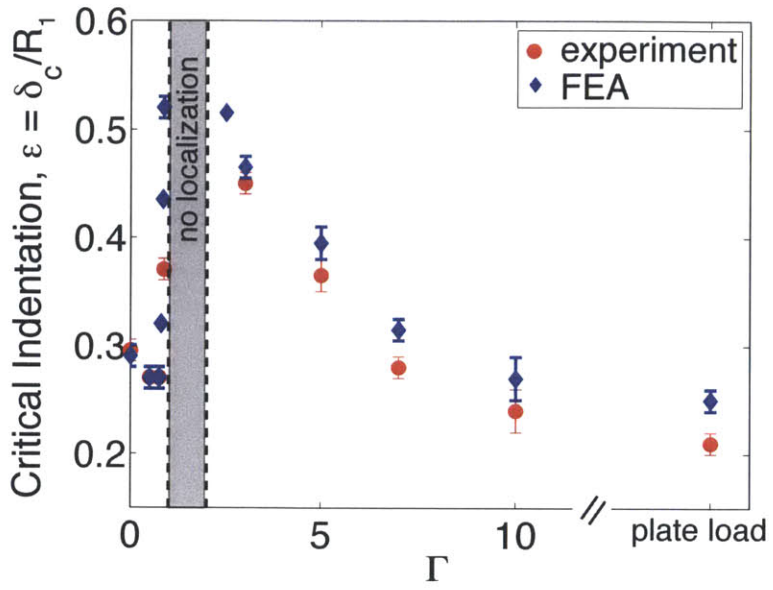

Figure 3-5: **Critical indentation.** Onset of localization versus the indenter-shell radii ratio, Γ. No localization occurs between $\Gamma = 1$ and $\Gamma = 2$ (indicated by the grey region, denoted as the *localization band gap*).

3.4 Geometry of the Shell-Indenter Contact

The indenter shape also effects the ridge-height, h, which we define as the vertical distance between the equator of the hemispherical shell, where it is clamped, and the point on the shell at which its surface inverts due to the indentation, thereby forming a ridge (see the schematics in Fig. 3-6a). In Fig. 3-6a), we plot this ridge-height measured experimentally (open symbols), as a function of indentation for point load, $\Gamma = 1$, $\Gamma = 3$, and plate load. For comparison, the corresponding data from the FEA (solid lines) is superimposed for the extreme cases of point and plate load. Even for large values of indentation, the ridge-height h decays approximately linearly with indentation, ϵ. Therefore the slope, $m = dh/d\delta$, can be measured and plotted as a function of the indenter's radii ratio, Γ, in Fig 3-6b). The ridge-height decreases the slowest for point indentation, with a rate of $m \sim -0.5$, and the fastest for plate load, with $m \sim -1$ (the ridge moves at the same rate as the indenter). For intermediate indenters ($0 < \Gamma < \infty$) the slope decreases monotonically with Γ and $-0.5 < m < -1$.

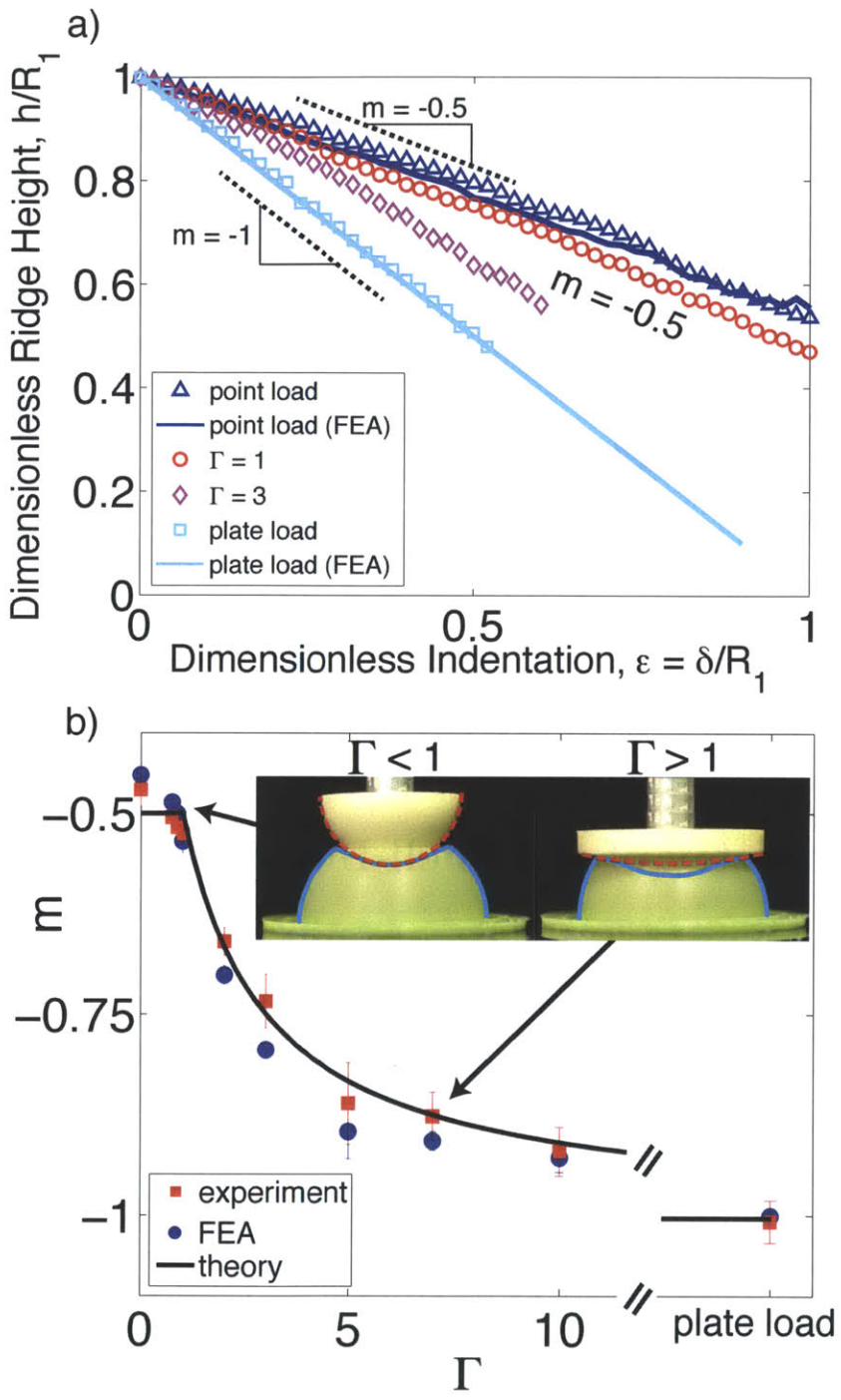

Figure 3-6: **Ridge-height.** a) Height of the ridge versus indentation for indenters with different geometries; experiments (data points) and simulations (solid lines). b) Slopes of ridge-height, m vs. indentation curves from experiments (red squares) and simulations (blue circles) indenters ranging from $\Gamma = 0$ to $\Gamma = \infty$. The theory line corresponds to the prediction from Eq. (3.6). Inset illustrates sharp and blunt indenters.

We now present a geometric argument that rationalizes these results. The schematic diagram in Fig. 3-7a illustrates the deformed configuration of the shell for $\Gamma < 1$. Here, the radius of the shell is $R_1 = h + \delta/2$, which in return gives

$$\frac{h}{R_1} = 1 - 0.5\left(\frac{\delta}{R_1}\right), \tag{3.1}$$

and yields the slope $m = dh/d\delta = -0.5$, for $\Gamma < 1$.

For $\Gamma > 1$, the nature of contact between the shell and the indenter is qualitatively different, as shown in the schematic diagram of Fig. 3-7b. Taking the radius of the indenter, R_2, into account and assuming small deformations, we obtain $R_1 = h + (\delta - \Delta)$, where Δ is the vertical distance between the pole of the indenter and the ridge-height, h (see schematic in bottom left of Fig. 3-6b). The vertical distance between the ridge-height h and the pole of the undeformed shell is Δ'. We construct a triangle (in blue in Fig. 3-7b) with the radius of the shell R_1, the radius of the indenter R_2, and the centerline that passes through the center points of the indenter and shell. We define α as the angle between the centerline and R_1, and β as the angle between the centerline and R_2. These angles (α, β) and the radii (R_1, R_2) are

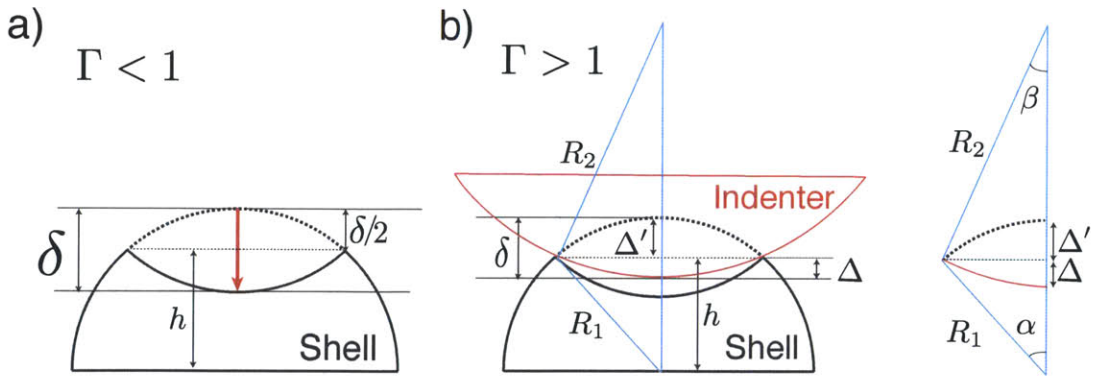

Figure 3-7: **Sharp vs. blunt indenter-shell contact.** a) Schematic for indentation with a sharp indenter, $\Gamma < 1$. b) Schematic for indention with a blunt indenter blunt indenters (indenter in red), $\Gamma > 1$. Blue triangle is constructed from the radius of the shell R_1, the radius of the indenter R_2, and the centerline that passes through the centers of the indenter and the shell.

related with a trigonometric relationship assuming the angles are small, such that $R_1\alpha = R_2\beta$. Using the trigonometric identity $2\sin^2\frac{\theta}{2} = 1 - \cos\theta$, we obtain:

$$\Delta = R_2(1 - \cos\beta) = 2R_2\sin^2\left(\frac{\beta}{2}\right). \tag{3.2}$$

For small values of the angle β, we get $\Delta = R_2\frac{\beta^2}{4}$. Similarly for Δ' and R_1, we get $\Delta' = R_1\frac{\alpha^2}{4}$. Now, we use the relationship $\delta = \Delta + \Delta'$ to obtain,

$$\frac{\Delta'}{\Delta} = \frac{\delta - \Delta}{\Delta} = \frac{R_1\alpha^2}{R_2\beta^2}. \tag{3.3}$$

Since we showed previously that $R_1\alpha = R_2\beta$, we can equate the ratio of radii to the ratio of angles $\Gamma = R_2/R_1 = \alpha/\beta$. Then, we can obtain the relation,

$$\Delta = \frac{1}{1+\Gamma}\delta. \tag{3.4}$$

By substituting this expression for Δ into our original expression for the radius of the shell, $R_1 = h + (\delta - \Delta)$, we obtain

$$R_1 = h + \delta\left[1 - \frac{1}{(1+\Gamma)}\right], \tag{3.5}$$

which yields the following slope for the h-δ curves,

$$m = \frac{dh}{d\delta} = -\left[1 - \frac{1}{1+\Gamma}\right]. \tag{3.6}$$

The dependence of m on Γ predicted by this geometric argument underlying Eq. (3.6) is plotted as the solid line in Fig. 3-6b and is found to be in excellent agreement with both the experimental and FEA data. This confirms that the variation in m is due to the different geometric nature of the indenter-shell contact proposed above, and which is explored in more detail next.

3.5 Role of Friction in the Mechanical Response

In order to achieve the excellent agreement between experiments and simulations highlighted above, we had to treat the shell-indenter interaction with care, and assume a frictional contact, while neglecting adhesion. This is even more important since, as we saw in the previous section, the nature and morphology of the shell-indenter contact varies for different values of Γ; from sharp indenters to blunt indenters. To stress the importance of friction, we now focus on the mechanical response during the indentation process, as quantified by the indentation load, P, as a function of indentation, ϵ. A series of $P - \epsilon$ curves, for increasing values of Γ, is presented in Fig. 3-8. For small indentation, there is a linear regime significant of the shell's stiffness, as previously described by [35, 62]. For large indentations, all curves with $\Gamma < 1$ eventually asymptote to an approximately constant value. In contrast, the various curves with $\Gamma > 1$ exhibit an inflection point and fan out; higher values of Γ result in higher loads.

Again, we observe a quantitative difference between sharp and blunt indenters.

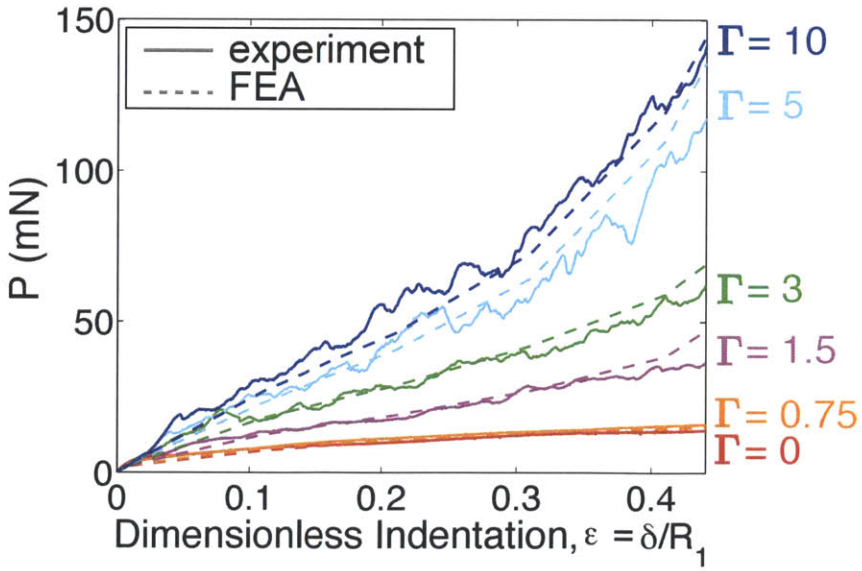

Figure 3-8: **Mechanical response and effect the shape of the indenter.** a) Force-indentation curves from experiments (solid lines) and finite element simulations (dashed lines) for a variety of indenters. Coefficients of friction for $\Gamma = 0, 0.75, 1.5, 3, 5, 10$ are, respectively, $\mu = 0, 1.5, 1.2, 1.7, 1.5$

For $\Gamma > 1$, a significantly higher load is required to indent a shell when compared with sharp indenters ($\Gamma < 1$) due to the different nature of the indenter-shell contact. For sharp indenters, the poles of the indenters and the shells remain in contact throughout indentation. On the other hand, for blunt indenters, the shell delaminates from the pole of the indenter, and pushes onto the shell at its ridges. This requires a substantially higher force level (as high as a factor of 10 for $\epsilon = 0.4$, when comparing $\Gamma = 0$ and $\Gamma = 10$) and also involves sliding and rolling of the two surfaces. These two scenarios are illustrated in the inset of Fig. 3-6b.

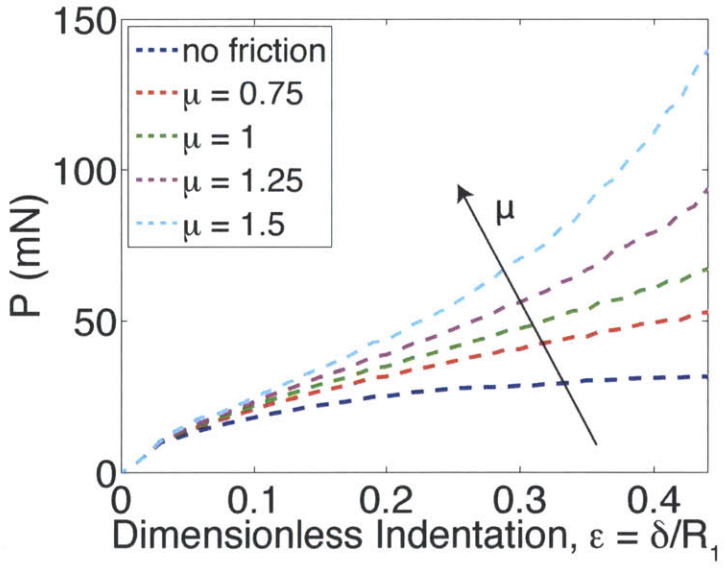

Figure 3-9: **The effect of friction on the mechanical response.** Force-indentation curves from simulations for $\Gamma = 10$ for no friction and a variety of friction coefficients.

From the detailed comparison between the experimental and FEA force-indentation curves, we have learned that friction plays an essential role on the mechanical response. Force-indentation curves from simulations without friction showed a significantly lower mechanical response than what was measured experimentally. As presented in Fig. 3-9), when the coefficient of friction μ is increased, the load required to indent the shell is also significantly increased. For example, at $\epsilon = 0.45$, the load required to indent a shell for $\mu = 1.5$ is increased by a factor as large as 5, when compared to doing so for a frictionless indenter-shell contact. Using an independent friction sliding test (details in Chapter 2), the friction coefficient was experimentally measured to be $\mu = 1.46 \pm 0.53$. The large variation in this measured value can be attributed to the fact that a dry friction description is oversimplistic for polymer-polymer surface contacts. Still, in the FEA, μ has been treated as a fitting parameter, bound within the measured experimental range (each values of μ for each indenter are listed in Table 3.1).

Γ	μ
0	0
0.05	1.5
0.75	1.5
0.8725	1.5
1	0
1.5	1.2
2	1.2
3	1.2
5	1.7
7	1.5
10	1.5
plate load	1.7

Table 3.1: **Friction coefficients for each indenter.** Friction coefficients μ used in FEA simulations for each value of Γ

This is appropriate since the experimental friction coefficients for each of the individual indenters are not precisely known due to the varying levels of roughness for indenters of different curvature, imparted by the fabrication process and set by the resolution of the CNC milling process.

Chapter 4

Numerical Exploration of Parameter Space

Given the predictive power of the numerics demonstrated in the previous chapter, we proceed by taking advantage of numerical simulations to conduct numerical experiments that are difficult to implement in the physical experiments. We first conduct a series of studies to demonstrate the prominence of geometry in the indentation of shells. To this end, we show that self-weight of the shell has minimal effect and that localization in shells is independent of the shell size. Additionally, we quantify the maximum principle strains and show that elastic and Neo-Hookean models produce nearly identical results, due to the fact that material non-linearities are negligible at small strains. We then investigate how the ratio between the thickness and the radius of the shell, t/R_1, effects the emergence and evolution of s-cones. Motivated by our previous observation that friction plays an important role, we further investigate the role of friction in localization.

4.1 Effect of Self-Weight

We begin by investigating the effect of the self-weight of the shell on the mechanical response. In particular, we study the case of point indentation for a shell with the same geometric and material parameters as the experiments and FEA simulations in

Chapter 3. In Fig. 4-1 a), we plot two load-displacement curves; the curve in red corresponds to a model that excludes the weight of the shell, and the curve in blue corresponds to a model that includes the self-weight of the shell. The vertical dashed lines indicate critical indentations at which 3 and 4 s-cones form. For small indentations, both curves exhibit nearly the same load under indentation, demonstrating that the weight of the shell has little effect in the indentation regime before s-cones form. The two curves start deviating from each other once s-cones first emerge. We quantify the deviation between the two curves by the ratio of the difference and the mean, φ, between the two curves at each value of indentation, shown in Fig. 4-1 b). The ratio φ remains small (approximately less than 10%), especially for the values of indentation of interest ($\epsilon = 0.21$ and $\epsilon = 0.67$) where s-cones form and evolve. Given that the effect of weight appears to have little effect on the mechanical response, we choose to neglect it in the studies that follow.

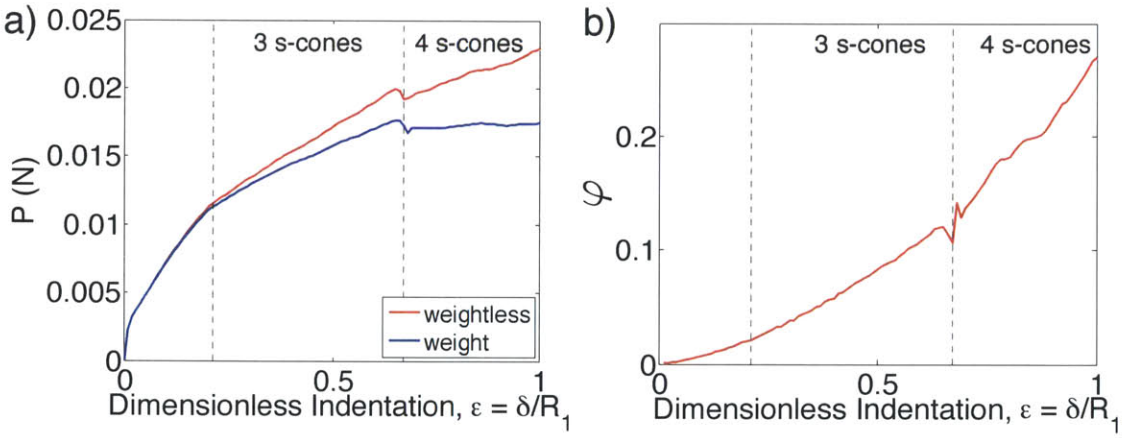

Figure 4-1: **The effect of self-weight on the mechanical response.** a) FEA force-indentation curves for a shell under point load indentation when weight is included (blue) or excluded (red) b) The ratio of the difference to the mean, φ, of the two force-indentation curves. The vertical dashed lines correspond to indentation values at which 3-scones and 4-scones form.

4.2 Varying the Radius of the Shell

To verify the universality of localization across lengthscales, i.e. to show that shells can be expected to have a similar response to indentation regardless of scale, we study the effect of the shell size (radius) on the formation of s-cones and also the mechanical response. In Fig. 4-2, we present a series of non-dimensionalized FEA load-indentation curves for shells under point indentation with various radii ranging from $R_1 = 0.01$ m to $R_1 = 1000$ m. The thicknesses of the shells is set such that the thickness to radius ratio, $t/R_1 = 0.01$, remains the same across all the shells considered in this part of the study. Upon non-dimensionalization of the indentation loads by Et^2 (E is the Young's modulus and t is the thickness of the shell), the load-indentation curves collapse onto a single master curve, indicating that the load response is scaleable for shells of different radii, given that the thickness to radius ratio, t/R_1, is kept constant.

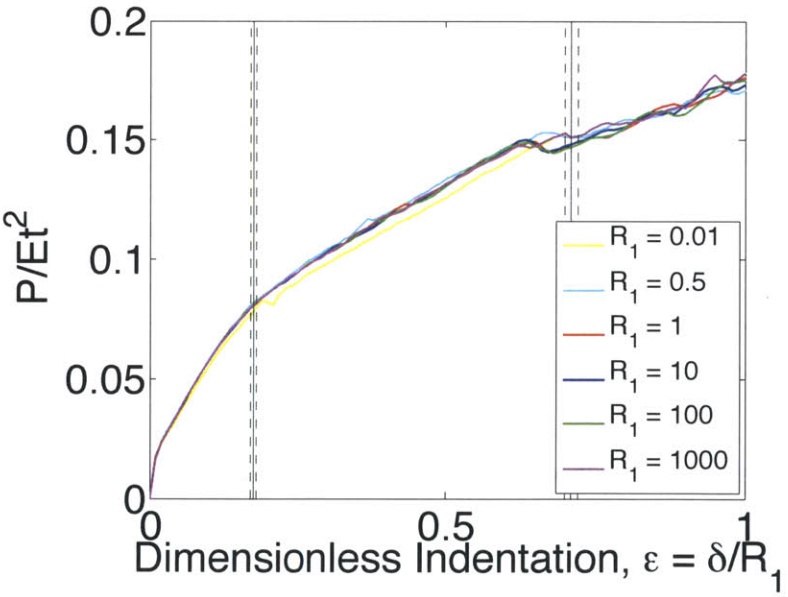

Figure 4-2: **The effect of shell radius on mechanical response.** Non-dimensionalized force-indentation curves for shells with various radii, ranging from $R_1 = 0.01$ to $R_1 = 1000$ with the same thickness ratio of $t/R_1 = 0.01$. Force is non-dimensionalized with the Young's modulus E and the thickness t. The solid vertical lines correspond to the average critical indentation (across the various shell radii) for the formation of 3 and 4 s-cones. The vertical dashed lines correspond to the standard deviation.

In addition to the mechanical response, the critical indentations for the onset of both 3 and 4 s-cones is plotted in Fig. 4-2; solid vertical lines correspond to the average critical indentation (across the various shell radii) and the vertical dashed lines correspond to the standard deviation. The critical indentations for $n = 3$ s-cones ($\epsilon = 0.18 \pm 0.005$) and $n = 4$ s-cones ($\epsilon = 0.71 \pm .01$) are nearly identical across the varying shell radii, with small standard deviations from the average values, further demonstrating the universality of localization across lengthscales.

4.3 Maximum Strains

We now quantify the shell's maximum principle strains, defined locally at the material level, in the shells as they are indented. This is important to consider in scenarios where measures of strain are needed for yield criteria (such as in plasticity) or for quantifying the effect of material non-linearities (such as in hyperelastic materials). The maximum principle strain is the maximum strain in the principal coordinate system, which is a measure of the maximum stretch (since there are no shear strain components in this frame). The principal strains are difficult to obtain in physical experiments and would have required 3D Digital Image Correlation (DIC), so we take advantage of FEA simulations to obtain these quantities.

In Fig. 4-3a), the maximum principle strain is plotted for a variety of sharp indenters (with $\Gamma \leq 1$). For each of the indenters, the maximum principle strain increases with indentation. For sharp indenters, the maximum principle strain is greatest for point load, and decreases as Γ increases towards 1. In Fig. 4-3 b), the maximum principle strain is plotted for a variety of blunt indenters (with $\Gamma > 1$). For blunt indenters, we see the opposite trend and find that the maximum principle strain is maximum for plate load and decreases as Γ decreases towards 1. The curves for the the maximum principle strain with respect to indentation sharply increase after the critical indentation points (indicated by black diamonds) for blunt indenters. For all the indenters, the maximum principle strains remain small and do not exceed 6%. It is remarkable that although the shells undergo significantly large macroscopic com-

pression under indentation, the local strains remain of the order of a few percent, albeit still localized. Given that the strains are small and the shell is thin (the thickness to radius ratio is small), the use of Kirchoff theory (as employed in the FEA simulations) is appropriate. Kirchoff theory is only valid for thin shells and small local strains, i.e. for scenarios in which transverse shear deformations are negligible [16].

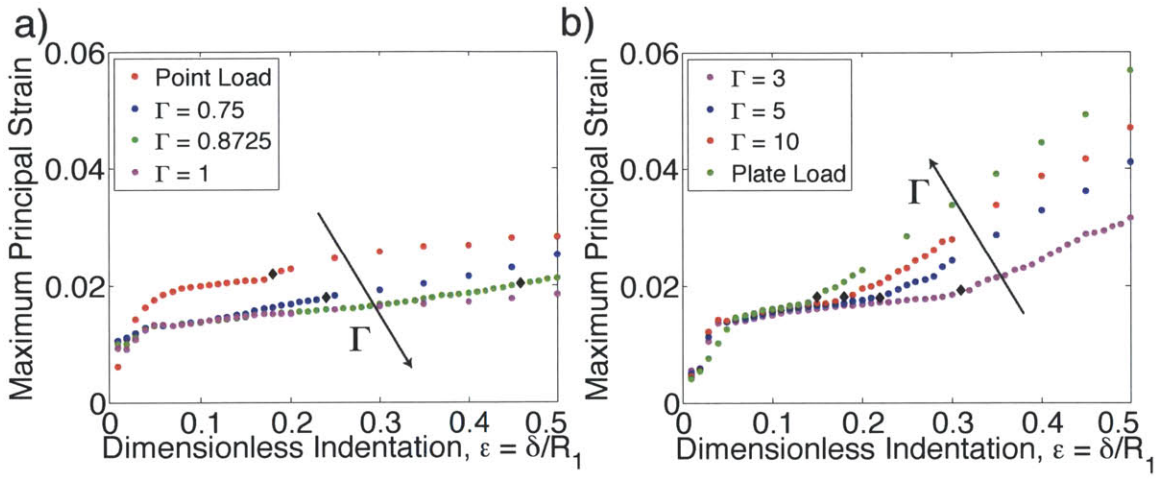

Figure 4-3: **Maximum Principal Strains** a) Maximum principal strains as a function of indentation for sharp indenters (with $\Gamma \leq 1$). Black diamonds indicate the critical indentation for the formation of s-cones for each of the indenters. b) Same for blunt indenters (with $\Gamma > 1$).

4.4 Comparison of Elastic and Neo-Hookean Material Models

The experiments and simulations in the previous chapter were conducted using a Neo-Hookean model, which is appropriate for rubbery materials, such as elastomeric VPS, that are non-linearly elastic. This is in contrast with previous studies on localization in thin shells which used a linear elastic elastic material model [36, 51]. We continue by comparing linear elastic and Neo-Hookean material models to understand the role of material non-linearities in localization. Two sets of FEA simulations are conducted, one with an elastic model and one with a Neo-Hookean model. In both models, the

material parameters were obtained from mechanical tests of the VPS polymer (details are in Chapter 2). In Fig. 4-4 we present a series of FEA snapshots for shells for a variety of shell-to-indenter radii, Γ, ranging from point load ($\Gamma = 0$) to plate load ($\Gamma = \infty$). Each of the corresponding snapshots in the FEA and elastic models are taken from the same values of indentation, ϵ. As in experiments before, s-cones are identified by sharp corners, but with the added value that in FEA simulations, we can also identify them with a sharp increase in energy density. Qualitatively, the elastic and Neo-Hookean models produce identical results, with the same number of s-cones forming for each of the indenters. As we saw in Chapter 3, localization occurs for all the indenters, except for $\Gamma = 1$, where the curvature of the indenter is identical to that of the shell and the two surfaces remain in complete contact, preventing the formation of s-cones. For sharp indenters with $\Gamma < 1$, there is an evolution in the number of s-cones that form with indentation, whereby the transition occurs when new s-cones emerge by splitting from previous ones. In contrast, for blunt indenters with $\Gamma > 1$, there is no evolution in the number of s-cones that form under indentation. This observation differs from what is seen in the FEA simulations and experiments presented in Chapter 3, where friction is included in the model. It could be possible that this discrepancy is a consequence of excluding friction in this part of the study.

To further compare the linear elastic and Neo-Hookean material models, we compare how the critical indentation changes with indenter geometry for both cases. In Fig. 4-5, the critical indentation is plotted as a function of Γ. As we saw in Chapter 3, the critical indentation has a divergence-like behavior around $\Gamma \sim 1$, where the critical indentation is maximum for the values of Γ on either side. The critical indentation decreases as $\Gamma \to 0$ or $\Gamma \to \infty$. Again, we find nearly identical quantitative results between the two material models, with the deviation between the two being within 2%.

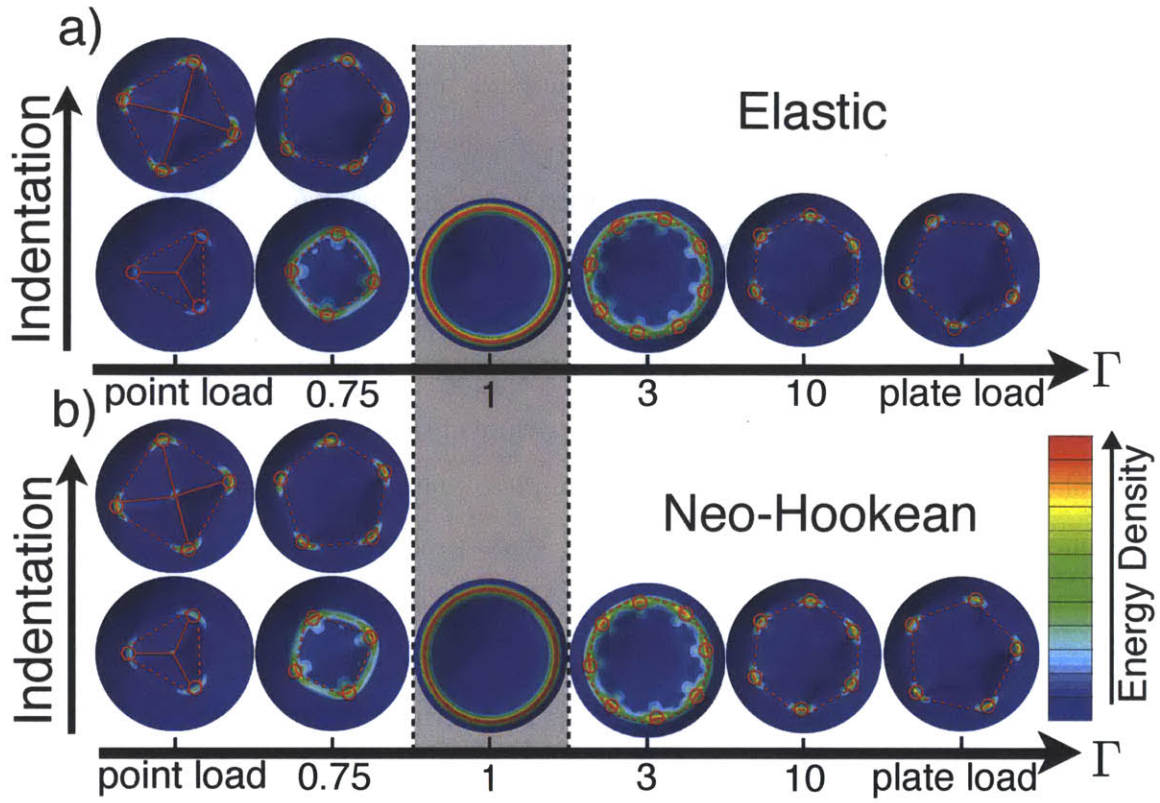

Figure 4-4: **Comparing elastic and Neo-Hookean Models** a) Snapshots from FEA simulations for an elastic shell indented at the pole for a variety of indenters, ranging from point load ($\Gamma = 0$) to plate load ($\Gamma = \infty$). b) Scenario with snapshots for FEA simulations for a Neo-Hookean shell at the same values of ϵ. The color map corresponds to strain energy density. Red circles indicate the location of s-cones. Dashed lines are drawn over ridges that connect s-cones along where the shell is inverted. Solid red lines are drawn over gullies that connect s-cones to the pole of the shell (only present for point load). No localization (indicated by the grey area) occurs with indenters with $\Gamma \sim 1$.

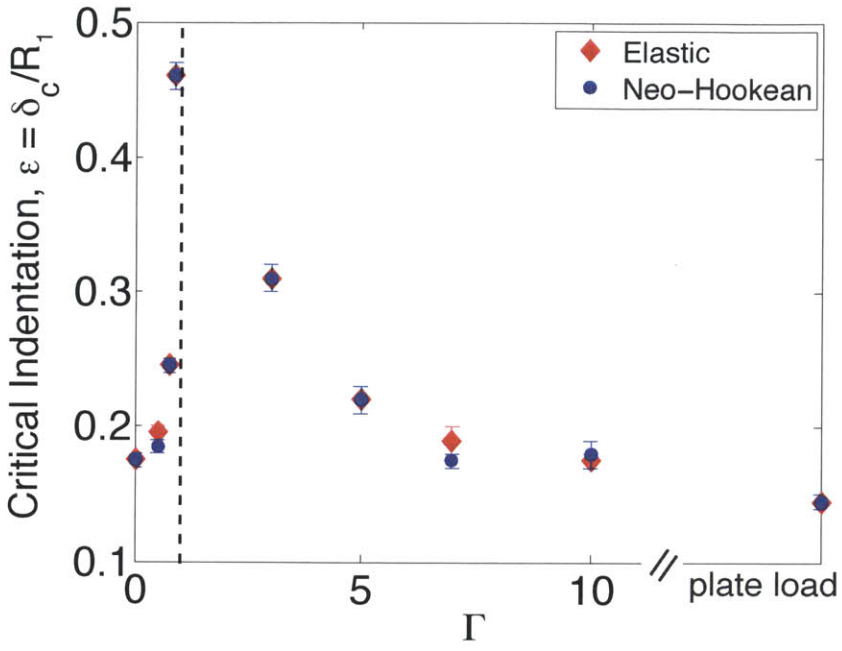

Figure 4-5: **Critical Indentation for elastic and Neo-Hookean models** for the onset of localization comparing Neo-Hookean and elastic models. No localization occurs for $\Gamma = 1$ (indicated by the vertical dashed line).

An additional way to quantitatively compare the elastic and Neo-Hookean models is through the mechanical response, as measured by the indentation load, P, as a function of indentation, ϵ. In Fig. 4-6, load-indentation curves are plotted for indenters over a range of values of Γ. For all indenters, the load monotonically increases with indentation and the curve has a concave-down shape. This observation is in contrast with the load-indentation curves from FEA simulations and experiments where friction is included in the model (discussed in Chapter 3 in Fig. 3-8), where the curves for $\Gamma > 1$ have a concave-up shape. Again, we see nearly identical quantitative results between the two material models.

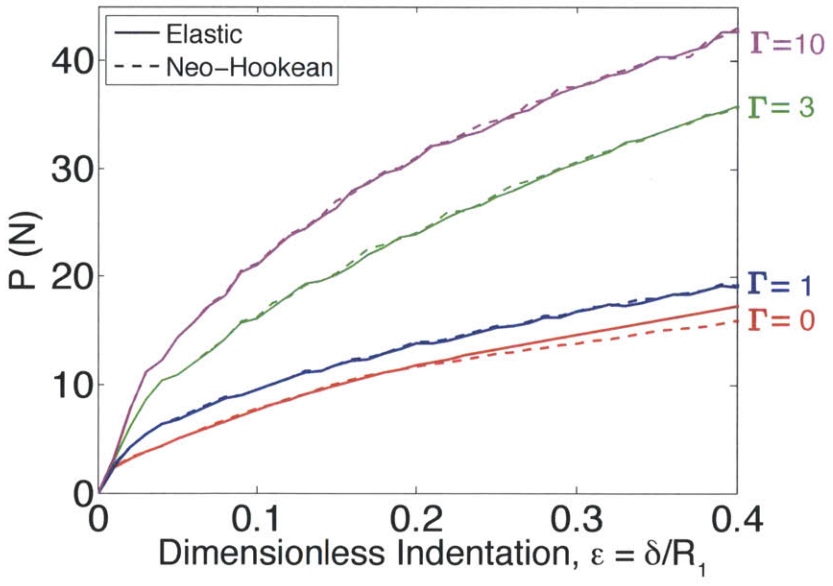

Figure 4-6: **Comparison mechanical response between elastic and Neo-Hookean models** Load-indentation curves for a variety of indenters ($\Gamma = 0$, $\Gamma = 1$, $\Gamma = 3$, and $\Gamma = 10$) from FEA simulations using an elastic model (indicated by solid lines) and a Neo-Hookean model (indicated by dashed lines).

Combining the three quantitative comparisons conducted thus far, i) morphology of the shells under indentation through the number of s-cones that form, ii) critical indentation, and iii) mechanical response, we conclude that the elastic and Neo-Hookean models produce nearly indistinguishable results. Although the shells undergo large macroscopic deformations under indentation, the maximum principal strains remain small, and thus the material non-linearities that play a role at higher strains for hyperelastic materials are negligible at these low strains. The mechanical testing data for VPS in Chapter 2 in Fig. 2-2 shows that the mechanical response is linear at the levels of strain measured in the simulations (below 6%). Because of this, the elastic and Neo-Hookean models are nearly indistinguishable in modeling thin shells under indentation.

The fact that we found such low values of strains despite the large macroscopic deformations suggests that s-cones, ridges, and gullies could be utilized as a natural designs for energetically efficient hinges, which could be useful to devise folding

origami-like shell structures. Additionally, our findings suggest that these results are not just applicable to elastomeric materials, but also extend to other materials within their elastic response, as long as the yield strains are not so low so that plasticity must be taken into account (which would be the case for metals, which yield at small strains, $\sim 1 - 2\%$).

4.5 Varying Thickness

We now consider the effect of the dimensionless thickness of the shell as characterized by the ratio of the thickness to the radius, t/R_1. FEA simulations are conducted for shells under point indentation with a variety of t/R_1 ratios ranging from 0.001 to 0.07. The ratio t/R_1 is varied by keeping $R_1 = 1$ m constant and varying the thickness t. In Fig. 4-7 we present a series of representative snapshots of shells with a range of t/R_1 values for which the formation and evolution of s-cones qualitatively differ. For shells of intermediate t/R_1 ratios, for example, $t/R_1 = 0.005$, 0.01, and 0.02, three s-cones form under point indentation, and later there is a splitting of an s-cone to form four s-cones in total, similar to the scenario presented for point indentation in Chapter 3. For the thinner shells, with $t/R_1 = 0.001$, 0.002, 0.003, and 0.004, there is a further splitting of s-cones such that five s-cones form upon further indentation after one of the four s-cones splits. For the thicker shells, with $t/R_1 = 0.03$, 0.04, 0.05, and 0.06, the maximum number of s-cones that forms is three, with no further evolution in the number of s-cones with indentation. For the thickest shell tested, with $t/R_1 = 0.07$, the deformation remained axisymmetric and no s-cones form.

FEA simulations are now used to quantify the effect of shell thickness on strain energy localization. In Fig. 4-8 b), the strain energy density, $\mathcal{E}$, is plotted along paths traced over ridges between adjacent s-cones for shells of various t/R_1, ranging from $t/R_1 = 0.002$ to 0.03, for shells indented to $\epsilon = 0.75$ under point load. Examples of these paths between adjacent s-cones are depicted with black dashed lines in Fig. 4-8 a). As the t/R_1 ratio decreases, energy localization increases at the s-cones relative to the ridges. For thinner shells, energy is focused more sharply at s-cones in comparison

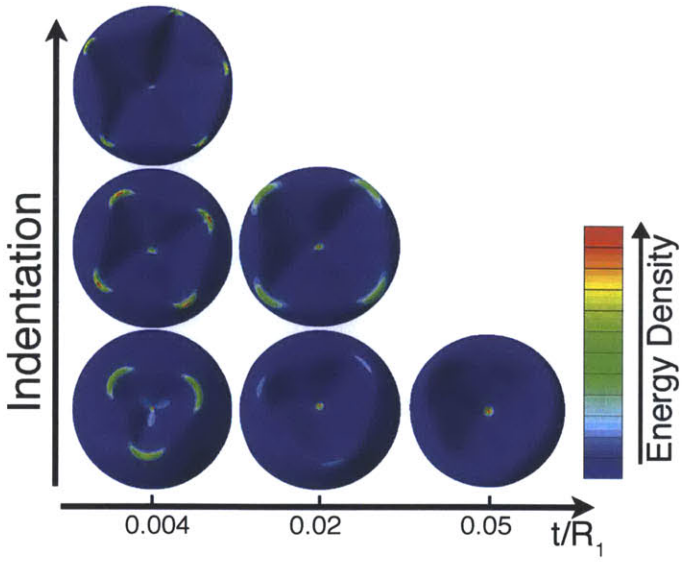

Figure 4-7: **The effect of shell thickness on the formation and evolution of s-cones.** Representative snapshots of shells with a range of t/R_1 values $(0.004, 0.02,$ and $0.05)$, as they evolve under point indentation. The color map corresponds to strain energy density.

to thicker shells. The sharpness of the energy focusing is quantified in Fig. 4-8 c) by plotting the minimum and maximum energy density, $\mathcal{E}_{min}$ and $\mathcal{E}_{max}$, as a function of t/R_1. These quantities are useful for comparing the localization at s-cones and at the center of the ridge, where the strain energy density is maximum and minimum, respectively. The energy density at the s-cones, $\mathcal{E}_{max}$ does not vary much with t/R_1 (stays within the range of $\sim 10^3\ J/m^3$) in comparison to the energy at the ridges, which increases significantly with t/R_1 and spans four decades. The simulation data is consistent with a power law with a slope of 2, suggesting an $\mathcal{E}_{min} \sim (t/R_1)^2$ scaling. As t/R_1 increases, strain energy becomes less localized at the s-cones in comparison to the ridges as the difference between the energy at the ridges and the energy at the s-cones decreases.

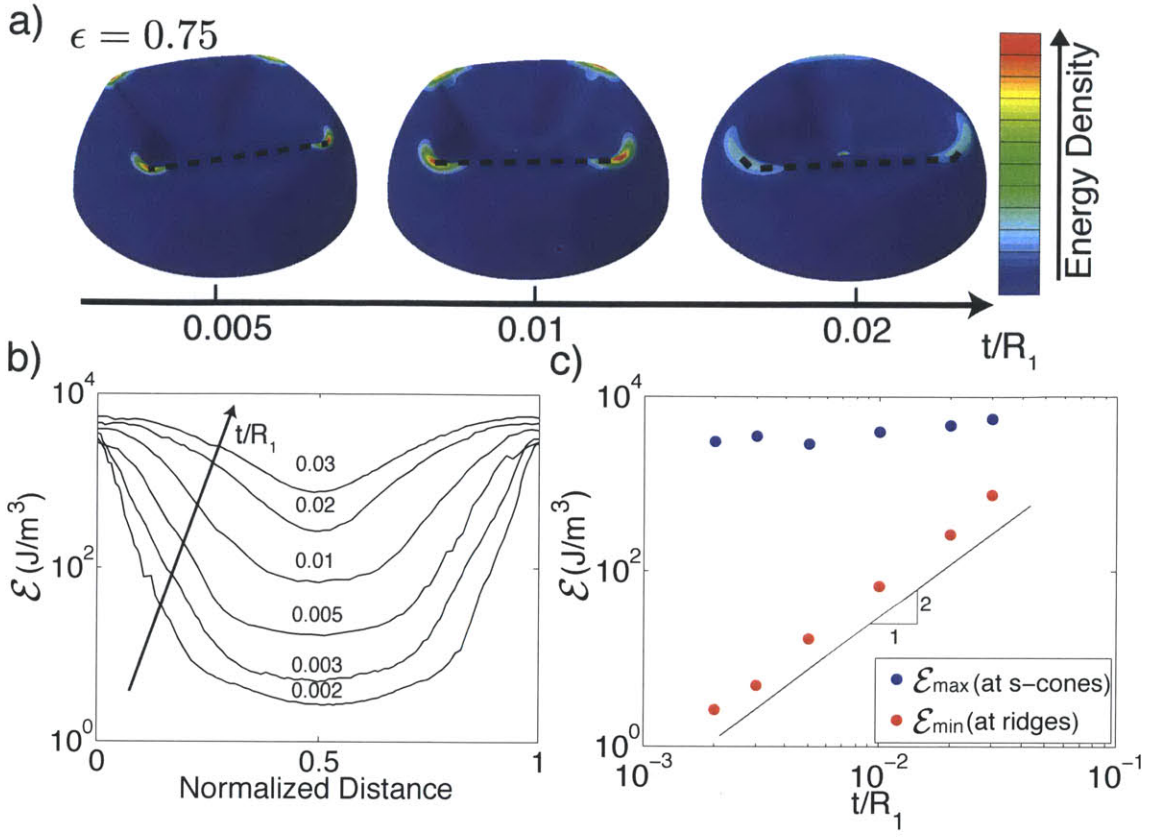

Figure 4-8: **The effect of shell thickness on energy localization** a) FEA snapshots of shells with various t/R_1 ratios under point indentation at $\epsilon = 0.75$. The color map indicates strain energy density. The black dashed lines trace a path along ridges between adjacent s-cones. b) Strain energy density $\mathcal{E}$ plotted along paths over ridges between adjacent s-cones for shells with various t/R_1 ratios, varying from $t/R_1 = 0.002$ to 0.03 for shells indented to $\epsilon = 0.75$ under point indentation. c) $\mathcal{E}_{max}$ (at the s-cones) and $\mathcal{E}_{min}$ (at the ridges) along the paths plotted to the left, as a function of t/R_1. The black line indicates a power law with an exponent 2 which is consistent to the simulation data.

Additionally, we quantify the effect of thickness on localization by studying the effect of t/R_1 on the critical indentation, the indentation at which s-cones form, which is plotted in Fig. 4-9. We compare two sets of FEA simulations: one for the material parameters for VPS (plotted in red), and one for a considerably stiffer elastic material with a Young's modulus $E = 69$ GPa (plotted in blue). We find excellent agreement between the two sets of data, demonstrating the applicability of these results to soft and stiff materials, as well as hyperelastic and elastic materials. The critical indentation increases linearly with t/R_1, with a slope of 16.3 ± 0.5 for the VPS, and 16.3 ± 0.8 for the stiffer elastic material. We find good agreement for the slopes for the soft and stiff materials, despite the large magnitude in difference in the Young's modulus E. For thinner shells, s-cones form for relatively small indentation, whereas the onset of s-cones is delayed for thicker shells. The linear relationship between critical indentation and t/R_1 has been predicted by previous studies. Vella

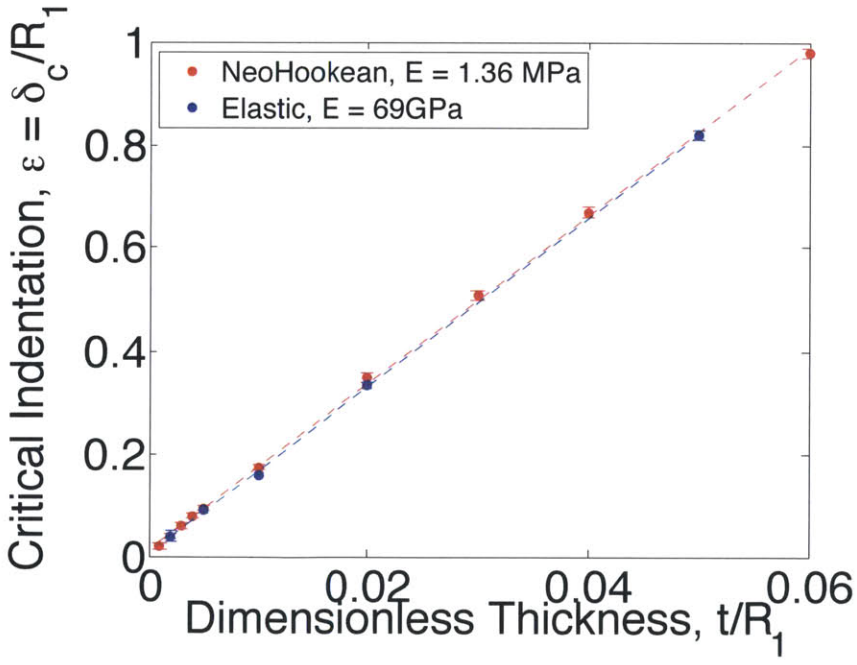

Figure 4-9: **The effect of shell thickness on critical indentation** for the onset of localization versus the ratio of shell thickness to radius, t/R_1. Red points and fitted line (with slope 16.3 ± 0.5) corresponds to FEA simulations using a Neo-Hookean model with the material parameters of VPS. Blue points and fitted line (with slope 16.3 ± 0.8) correspond to FEA simulations using an elastic model of a much stiffer material.

et al. [62] showed through non-dimensionalizing the governing equations that for shells in the weakly pressurized limit, the critical indentation for the formation of localized structures is linearly related to thickness. Through numerical studies, Vaziri [51] found the constant of proportionality to be 14, which is 16% smaller than the constant of proportionality measured in this study.

4.6 Effect of Friction

Previously in Chapter 3, we showed that friction has a significant effect on the mechanical response and that it was essential to assume a frictional shell-indenter contact in the FEA model, in order to produce good agreement with the experiments. Motivated by this discovery of the importance of friction, we further investigate the role of shell-indenter frictional contact in the indentation of shells. A series of FEA simulations are conducted for $\Gamma = 10$ with a variety of friction coefficients ranging from $\mu = 0$ to 1.7. Friction plays a particularly important role for blunt indenters, thus $\Gamma = 10$ was chosen as a representative blunt indenter for this study. We leave it to a future study to conduct a systematic invesetigation of the effect of Γ on frictional contact.

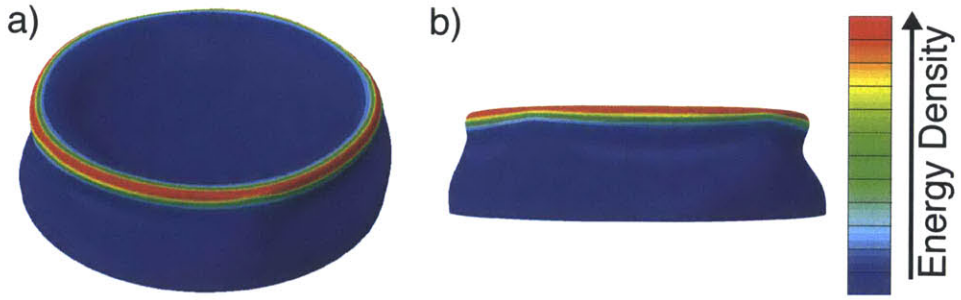

Figure 4-10: **Global buckling** a) Isometric view of a shell exhibiting a global buckling mode under large indentation (configuration shown at $\epsilon = 0.51$) for an indenter with $\Gamma = 10$ and a high friction coefficient $\mu = 1.7$. b) Side view. Color map indicates strain energy density.

For the low friction coefficients, $\mu = 0,\ 0.25,\ 0.5$, and 0.75, six s-cones form under indentation. The number of s-cones that develop increases to seven for higher friction coefficients $\mu = 1,\ 1.2$, and 1.3 and to 8 s-cones for $\mu = 1.4$. Select snapshots of the shells from FEA simulations showing six, seven, and eight s-cones for different values of the friction coefficient μ and the same value of indentation $\epsilon = 0.4$ are shown in Fig. 4-13. For the highest friction coefficients, $\mu = 1.5$ and 1.7, the deformation remains axisymmetric and no s-cones appear. For $\mu = 1.7$, the shell undergoes global buckling under high indentation, in which the sides of the shell cave inwards near the base of the shell, forming a pattern of five horizontal dimples (shown in Fig. 4-10).

Next, we quantify the critical indentation for the onset of localization as a function of the friction coefficient μ, plotted in Fig. 4-11a. The formation of s-cones is delayed with the increase in the friction coefficient μ. The critical indentation asymptotes to $\epsilon = 0.18$, as μ decreases towards 0. Additionally, we plot the reaction force at the critical indentation as a function of μ (Fig. 4-11b). Similar to the critical indentation as a function of μ, the reaction force at the critical indentation increases with μ and asymptotes to 30 N as μ decreases towards 0. These two results suggest that rougher shells, therefore with a higher friction coefficient μ, are stronger and more resistant to localization.

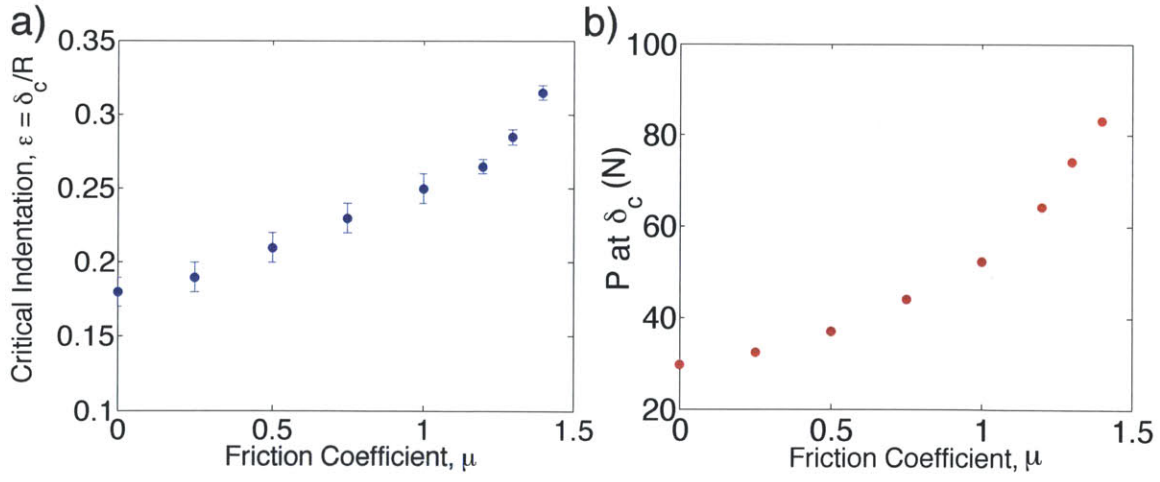

Figure 4-11: **The effect of friction on the critical indentation** a) The critical indentation for the onset of localization for an indenter with $\Gamma = 10$ for a range of friction coefficients μ. b) Reaction force, P, at the critical indentation, for a range of friction coefficients μ.

We also quantify the effect of friction on the mechanical response, as measured by load-indentation curves (Fig. 4-12) for $\Gamma = 10$ for a variety of friction coefficients μ. The load significantly increases with the friction coefficient μ. For small friction coefficients $\mu < 1$, the load-indentation curve has a concave-down shape in which the load asymptotically approaches an approximately constant value. In contrast, for large friction coefficients $\mu > 1$, the load-indentation curve has an inflection point after which the curve has a concave-up shape.

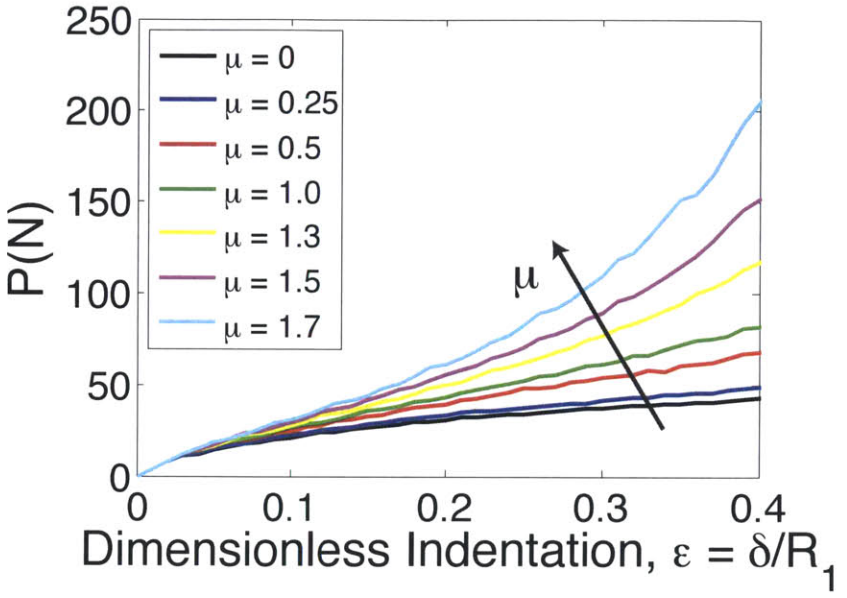

Figure 4-12: **The effect of friction on the mechanical response** load-indentation curves for an indenter with $\Gamma = 10$ for a variety friction coefficients μ.

The effect of friction is now quantified through the strain energy density, $\mathcal{E}$. In Fig. 4-13 b), $\mathcal{E}$ is plotted over paths traced over ridges between s-cones. As the friction coefficient μ increases, energy becomes less sharply focused at s-cones relative to the ridges. In Fig. 4-13 c), the maximum and minimum energy density along the paths are plotted as a function of the friction coefficient μ. These quantities, allow us to compare the energy focusing at the s-cones (corresponding to $\mathcal{E}_{\max}$ and at the ridges (corresponding to $\mathcal{E}_{min}$). As the friction coefficient μ increases, the energy at the s-cones decreases and the energy at the ridges increases. The energy at the s-cones and energy at the ridges appear to asymptote towards the same value ($\sim 2 \times 10^3 J/m^3$) as

μ increases. As the the frictional contact between the shell and indenter increases, the energy becomes less localized at the s-cones relative to the ridges. With increasing μ, the energy becomes more evenly distributed along the ridges, eventually to the extent that s-cones are no longer distinguishable and the deformation is essentially axisymmetric (which is the case for the highest friction coefficients we tested, $\mu = 1.5$ and 1.7, where no s-cones are identified).

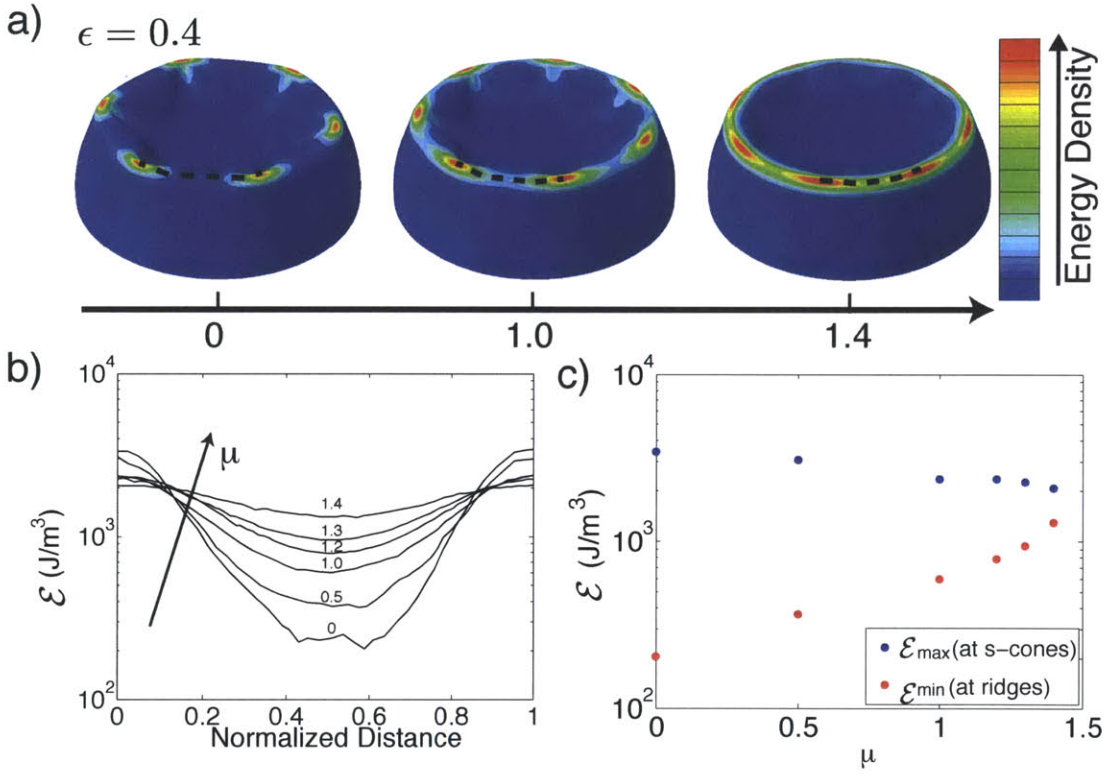

Figure 4-13: **The effect of friction on energy localization** a) Snapshots from FEA simulations for an indenter with $\Gamma = 10$ for various friction coefficients μ. The color map indicates strain energy density. The black dashed lines trace a path over ridges between adjacent s-cones. b) Strain energy density plotted along paths over ridges between adjacent s-cones for shells with various friction coefficients μ, ranging from $\mu = 0$ to 1.4 for shells indented to $\epsilon = 0.4$ for an indenter with $\Gamma = 10$. c) $\mathcal{E}_{max}$ (at the s-cones) and $\mathcal{E}_{min}$ (at the ridges) along the paths plotted to the left, as a function of μ.

Chapter 5

Conclusions and Discussion

5.1 Summary and Discussion of Findings

Using both precision desktop-scale model experiments and finite element numerical simulations, we have presented a rich scenario for the large deformation of a thin spherical shell under indentation. The curvature of the indenter was systematically varied and was found to have a strong effect on the onset and evolution of localized structures. A localization band gap region where no s-cones form and the deformation remains axisymmetric was found for indenters whose curvatures are near that of the shell. Just outside of the localization band gap, the number of s-cones that forms is maximum and decreases as the curvature of the indenter approaches zero (for point load) or infinity (for plate load). Around the localization band gap, the critical indentation for the onset of localization has a divergent-like behavior, where the onset of localization is significantly delayed as the curvature of the indenter approaches that of the shell. The nature of the contact between the shell and the indenter was found to be a crucial ingredient in the process. Geometry plays a prominent role in the shell-indenter contact, which was rationalized through a simple geometric argument that accurately described the effect of the curvature of the indenter on contact with the shell.

The nature of the shell-indenter contact was also found to be important in the context of friction, which we had to include in the finite element model in order to ar-

rive at the excellent agreement with the experiments. We found that friction between the indenter and the shell significantly affects the shells's load-bearing capacity, especially for blunt indenters ($\Gamma > 1$), which require significantly higher loads to indent shells compared to sharp indenters ($\Gamma < 1$). Through a systematic study of the effect of varying the friction coefficient μ, we observed that rougher shell-indenter contacts can lead to the suppression of localization, in which energy becomes more evenly distributed and the onset of localization is delayed. This finding, in conjunction with the observation of increased load-bearing capabilities for rough shell-indenter contact has implications for engineering scenarios, where the design of strong shells that resist localization can be enhanced by roughening their surfaces.

By varying the radius of the shell, while keeping the thickness-to-radius ratio t/R_1 constant, we demonstrated the scale-invariance of localization in shells, in the onset and evolution of s-cones. This finding demonstrates that our results are relevant and applicable for engineering scenarios across a wide range of lengthscales. Although the size of the shell does not play an important role, we also found that the thickness of the shell relative to its radius has a significant effect on localization. The onset and evolution of s-cones, and whether or not they form at all, strongly depends on the thickness of the shell. The extent of localization at the s-cones relative to the ridges, as measured by the strain energy density stored, is also strongly dependent on the shell thickness; energy is more strongly localized at s-cones for thin shells in comparison to thick shells.

Though shells can be subjected to large macroscopic deformation under indentation, we showed that the strains remain relatively small (less than $\sim 6\%$). Because material non-linearities for hyperelastic materials do not play a large role at such small strains, we observe nearly identical response to indentation for shells modeled with both linear elastic and Neo-Hookean materials. This observation suggests that our results are applicable beyond elastomeric materials and can be extended to other materials that remain in the elastic regime at these values of strain, provided that there is no plastic deformation at the levels of strains that are reached. The fact that large macroscopic deformations can be achieved with small strains suggests that

localized structures such as s-cones, ridges, and gullies can be employed as energetically efficient hinges, which could be applied to the design of folding origami shell structures.

5.2 Geometric Frustration Leads to Localization

Without a general predictive analytical model of the localization process at hand, we are lead to speculate that geometric frustration underpins the buckling transition from the axisymmetric state into the onset of s-cones. We propose that the mechanism is related to that recently reported by Dias *et al.* [63], who studied the mechanics of folding of an annular flat plate containing a concentric circular crease (a model of this from their paper is shown in Fig. 5-1). Folding the crease induces out-of-plane buckling of the plate. Further increasing the dihedral angle of the fold, results in increasingly more non-planar configurations and an increasing storage of stretching energy at the crease. If the annulus is cut, the geometric constraint is released, and it collapses into a planar state. Geometric and topological constrains, coupled with the mechanics of plates, dictate the permissible configurations in this scenario.

Similarly in our system, indentation introduces geometric frustration that disrupts the isometry of the shell's inverted cap. Once the circular ridge forms, the angle of the folded region where curvature of the shell inverts, increases as the shell is indented further which leads to a growing storage of strain energy at the ridge (the angle can be derived using an argument similar to that presented for the slope of the ridge-height vs. indentation curves, shown in Fig. 3-6). Past a critical indentation (quantified in Fig. 3-5) the circular ridge looses symmetry and due to its high energetic cost, stretching is focused onto localized structures, the s-cones. Understanding this interplay between geometric frustration and localized deformation could help rationalize our findings.

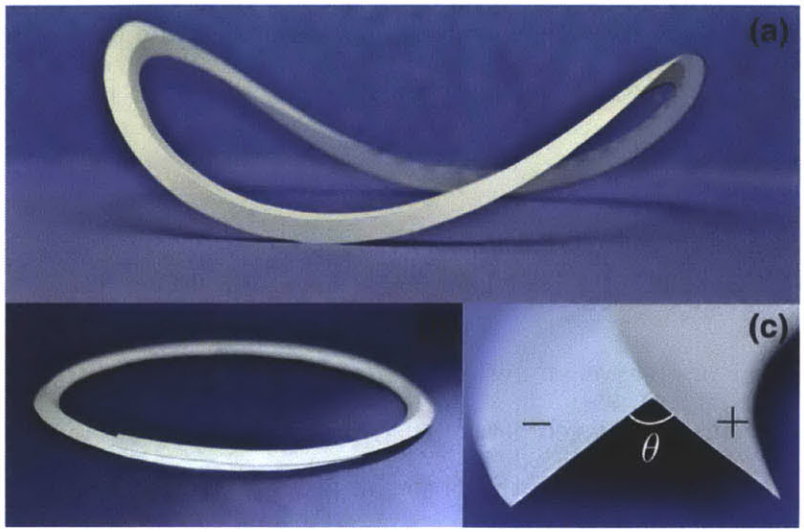

Figure 5-1: **Geometric frustration in an annular flat plate.** Fig. 1 from Dias *et al.* [63] a) An otherwise flat annular plate buckles out of plane when it is folded along its centerline. b) If the annulus is cut, it collapses into a planar state. c) A schematic with the dihedral angle θ of the fold between the left (-) and right (+) planes.

5.3 Analogy with Buckling of Confined Elastica

We observed that the number of s-cones at onset increases, when the curvature of the indenter approaches the shell's curvature towards $\Gamma \sim 1$, either from above or below. To comment on this observation, we establish an analogy with buckling of confined elastica. When a slender beam is compressed axially, but its transverse displacement is constrained by two confining walls [64, 65], high-order buckling modes can be excited (in contrast to the classic mode-one Euler buckling when the beam is unconstrained). In this case, the buckling wavenumber increases with the lateral confinement and the geometric constraint of the two confining walls is the driving mechanism for exciting high-order buckling modes. In Fig. 5-2 is an example of a sheet confined between two plates. With increased confinement, the sheet transitions from the first buckling mode to a mode-two buckling.

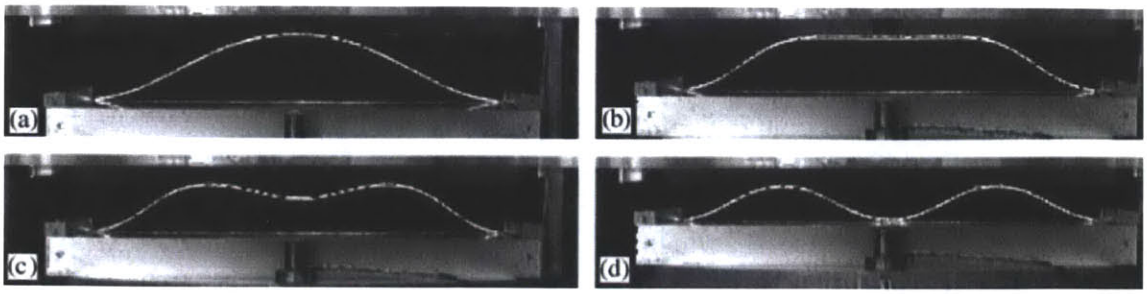

Figure 5-2: **Buckling of a confined sheet.** Fig. 2 from Roman and Pocheau [65]. A polycarbonate sheet confined between two plates transitioning from the first Euler buckling mode to a mode-two buckling as the plate is compressed.

Following this analogy and applying it to the indentation of shells, point load indentation in our problem can be considered as being unconstrained. At the other extreme of maximum constraint, when $\Gamma \sim 1$, the surfaces of the shell and indenter are in close contact with each other, preventing the shell from delaminating from the indenter, thereby precluding local buckling (no s-cones form). In the constrained Euler buckling analogy, this corresponds to the case where the two constraining plates are separated by a distance equal to the thickness of the strip such that buckling cannot occur. For $\Gamma > 0$, and outside the localization band gap in the neighborhood of $\Gamma \sim 1$, are cases of intermediate constraint, in which local buckling is allowed to occur, yet the shell-indenter contact constrains the buckling morphology. This constraint due to the shell-indenter contact excites higher order modes (increasing the number of s-cones) and affects the onset of localization, which is delayed as the indenter curvature approaches that of the shell.

5.4 Future Work and Potential Applications

Thus far we have only considered elastic and hyperelastic materials. In many engineering applications, such as in metallic structures, the effect of plasticity, which begins to play a role at small strains, is an essential ingredient to consider. There have been a number of studies on the buckling of spherical shells under indentation that

include the effects of plasticity [54, 66, 56, 52]. Similar to what is seen in elastic shells as in our study, deformation localizes and s-cones form. However, the added effect of plasticity leads to irreversible deformation and affects the formation of s-cones. Most studies focus on either point load or plate load indentation and do not consider indenters of intermediate curvatures, which are relevant for many engineering scenarios. A systematic study with the variation of the indenter curvature, similar to the one we have conducted in the present study, could be extended to materials that are subject to plastic deformation. We expect that a similar set of rich phenomenology would be found in such systems which would call for detailed quantitative predictions.

Furthermore, we have only considered quasi-static loading via indentation. There are a plethora of ways to load a shell, for many of which dynamic effects are important to include. For example, shell structures such as the bodies of cars and airplanes undergo dynamic loading during high speed collisions [12]. Moreover, shell structures, such as radomes and dome-shaped stadiums, are often subject to wind loading, which can lead to localized deformation [67]. Depressurization is another common loading mechanism, which has been considered in a number of recent studies [1, 47, 48, 49]. Our dual approach of desktop-scale model experiments and finite element modeling could potentially be explored beyond indentation and be applied to some of these alternative loading mechanisms. Through a systematic variation of the control parameters in these various loading mechanisms, we could gain insight into the essential physical ingredients involved in localization and also make a direct comparison with our scenario of indentation.

So far our study has only considered unpressurized shells. Vella *et al.* [68] recently conducted a theoretical and numerical study of the indentation of pressurized shells. They show that for shells that are unpressurized, or only weakly pressurized, polygonal localized structures (s-cones) form under point indentation. For increasing pressurization, there is a transition from s-cones to wrinkles. However, the focus of the study is mostly on wrinkling and not much is known about when and how one goes from polygonal localization to wrinkles. Our desktop-scale precision model experimental approach could contribute to these past studies, which have not yet used

experimental methods for systematic exploration. Our experiments would provide invaluable insight into the transition between polygonal localization to wrinkling.

Moreover, given the scale-invariance of the scenario presented here, our results should find uses for engineering applications at a large range of lengthscales. Of recent interest at the microscale is Atomic Force Microscopy (AFM). As the limits are pushed towards applying AFM to increasingly smaller objects, the curvature of the tip relative to the object being indented will be increasingly important to consider in measuring the mechanical response of objects at the micro-, or even nano-scale [62, 4]. Our insight into the role of geometry in shell-indenter contact could be applied to AFM to understand how the shape of the probe affects measurements, which would allow for a more accurate characterization of objects at smaller and smaller scales.

The robustness of the observed localization behavior and the excellent agreement found between experiments and numerics in this study suggest that there is an underlying mechanism at play that arises from the strong interplay between geometry and mechanics. However, we are still far from a full predictive understanding of the underlying mechanism for the observations we have made. We hope that our exploratory study will help catalyze further theoretical efforts in this direction.

Bibliography

[1] S. S. Datta, S.-H. Kim, J. Paulose, A. Abbaspourrad, D. R. Nelson, and D. A. Weitz, "Delayed buckling and guided folding of inhomogeneous capsules," *Physical Review Letters.*, vol. 109, p. 134302, Sep 2012.

[2] M. Arnoldi, M. Fritz, E. Bäuerlein, M. Radmacher, E. Sackmann, and A. Boulbitch, "Bacterial turgor pressure can be measured by atomic force microscopy," *Physical Review E*, vol. 62, pp. 1034–1044, Jul 2000.

[3] W. Roos, R. Bruinsma, and G. Wuite, "Physical virology," *Nature Physics*, vol. 6, no. 10, pp. 733–743, 2010.

[4] M. Baclayon, G. Wuite, and W. Roos, "Imaging and manipulation of single viruses by atomic force microscopy," *Soft Matter*, vol. 6, no. 21, pp. 5273–5285, 2010.

[5] F. Dubreuil, N. Elsner, and A. Fery, "Elastic properties of polyelectrolyte capsules studied by atomic-force microscopy and RICM," *The European Physical Journal E: Soft Matter and Biological Physics*, vol. 12, no. 2, pp. 215–221, 2003.

[6] J. Foucher, S. W. Schmidt, C. Penzkofer, and B. Irmer, "Overcoming silicon limitations: new 3d-afm carbon tips with constantly high-resolution for sub-28nm node semiconductor requirements," in *SPIE Advanced Lithography*, pp. 832432–832432, International Society for Optics and Photonics, 2012.

[7] W. H. Roos, M. M. Gibbons, A. Arkhipov, C. Uetrecht, N. Watts, P. Wingfield, A. C. Steven, A. J. Heck, K. Schulten, W. S. Klug, and G. Wuite, "Squeezing protein shells: how continuum elastic models, molecular dynamics simulations, and experiments coalesce at the nanoscale," *Biophysical journal*, vol. 99, no. 4, pp. 1175–1181, 2010.

[8] W. H. Roos, K. Radtke, E. Kniesmeijer, H. Geertsema, B. Sodeik, and G. J. Wuite, "Scaffold expulsion and genome packaging trigger stabilization of herpes simplex virus capsids," *Proceedings of the National Academy of Sciences*, vol. 106, no. 24, pp. 9673–9678, 2009.

[9] K. Costa and F. Yin, "Analysis of indentation: implications for measuring mechanical properties with atomic force microscopy.," *Journal of Biomechanical Engineering*, vol. 121, no. 5, p. 462, 1999.

[10] G. Wempner and D. Talaslidis, *Mechanics of solids and shells: theories and approximations*, vol. 24. CRC Press, 2002.

[11] X. Zhang, "Impact damage in composite aircraft structures-experimental testing and numerical simulation," *Proceedings of the Institution of Mechanical Engineers, Part G: Journal of Aerospace Engineering*, vol. 212, no. 4, pp. 245–259, 1998.

[12] W. Johnson and A. Mamalis, "Crashworthiness of vehicles," tech. rep., National Technical University of Athens, 1978.

[13] J. Zessin, W. Lau, and J. Ochsendorf, "Equilibrium of cracked masonry domes," *Proceedings of the ICE-Engineering and Computational Mechanics*, vol. 163, no. 3, pp. 135–145, 2010.

[14] J. Rayleigh, "The theory of sound, vols. 1 and 2," 1945.

[15] S. P. Timošenko, *History of strength of materials: with a brief account of the history of theory of elasticity and theory of structures.* DoverPublications.com, 1953.

[16] S. Timoshenko, S. Woinowsky-Krieger, and S. Woinowsky, *Theory of plates and shells*, vol. 2. McGraw-hill New York, 1959.

[17] R. Von Mises, "Der Kritische Aussendruck Zylindrischer Rohre," *Ver. Dtsch. Ing., Z*, vol. 58, pp. 750–755, 1914.

[18] R. Zoelly, *Ueber ein Knickungsproblem an der Kugelschale.* PhD thesis, Zürich, 1915.

[19] A. van der Neut, *De elastische stabiliteit van de dunwandigen bol.* PhD thesis, Delft, 1932.

[20] C. Biezeno, "Über die Bestimmung der Durchschlagkraft einer Schwachgekrümmten, Kreisförmigen Platte," *Zeitschrift für Angewandte Mathematik und Mechanik*, vol. 15, no. 1-2, pp. 10–22, 1935.

[21] J. Thompson, "The elastic instability of a complete spherical shell," *Aeronaut. Quart*, vol. 13, pp. 189–201, 1962.

[22] M. A. Krenzke, "Tests of machined deep spherical shells under external hydrostatic pressure," tech. rep., DTIC Document, 1962.

[23] A. Sabir, "Large deflection and buckling behaviour of a spherical shell with inward point load and uniform external pressure," *Journal of Mechanical Engineering Science*, vol. 6, no. 4, pp. 394–404, 1964.

[24] T. von Karman and H.-S. Tsien, "The buckling of thin cylindrical shells under axial compression," *Journal of the Aeronautical Sciences*, vol. 8, no. 8, pp. 303–312, 1941.

[25] R. Evan-Iwanowski, H. Cheng, and T. Loo, "Experimental investigations on deformations and stability of spherical shells subjected to concentrated loads at the apex," in *Proceedings of the Fourth US National Congress of Applied Mechanics*, pp. 563–575, 1962.

[26] L. Berke and R. Carlson, "Experimental studies of the postbuckling behavior of complete spherical shells," *Experimental Mechanics*, vol. 8, no. 12, pp. 548–553, 1968.

[27] E. Reissner, "Stresses and small displacements of shallow spherical shells," *Journal of Mathematical Physics*, vol. 25, no. 4, pp. 279–300, 1946.

[28] D. Ashwell, "On the large deflection of a spherical shell with an inward point load," in *Proceedings of IUTAM Symposium on the Theory of Thin Elastic Shells, Delft*, pp. 43–63, 1959.

[29] W. Koiter, "The nonlinear buckling problem of a complete spherical shell under uniform external pressure," *Proceedings of the Koninklijke Nederlandse Akademie van Wetenschappen. Series B: Palaeontology, Geology, Physics, Chemistry, Anthropology*, vol. 72, pp. 40–123, 1969.

[30] L. Landau and E. Lifshitz, *Theory of Elasticity, Vol. 7 of Course of Theoretical Physics, 2nd English ed.* Pergamon Press, 1970.

[31] A. Pogorelov, *Bendings of surfaces and stability of shells*, vol. 72. Amer Mathematical Society, 1988.

[32] B. Audoly and Y. Pomeau, *Elasticity and geometry: from hair curls to the nonlinear response of shells.* Oxford University Press Oxford and New York, 2010.

[33] D. P. Updike and A. Kalnins, "Axisymmetric behavior of an elastic spherical shell compressed between rigid plates," *Journal of Applied Mechanics*, vol. 37, no. 3, pp. 635–640, 1970.

[34] D. P. Updike and A. Kalnins, "Contact pressure between an elastic spherical shell and a rigid plate," *Journal of Applied Mechanics*, vol. 39, no. 4, pp. 1110–1114, 1972.

[35] A. Lazarus, H. C. B. Florijn, and P. M. Reis, "Geometry-induced rigidity in nonspherical pressurized elastic shells," *Physical Review Letters.*, vol. 109, p. 144301, Oct 2012.

[36] A. Vaziri and L. Mahadevan, "Localized and extended deformations of elastic shells," *Proceedings of the National Academy of Sciences*, vol. 105, no. 23, pp. 7913–7918, 2008.

[37] T. Witten, "Stress focusing in elastic sheets," *Reviews of Modern Physics*, vol. 79, no. 2, p. 643, 2007.

[38] A. E. Lobkovsky, "Boundary layer analysis of the ridge singularity in a thin plate," *Physical Review E*, vol. 53, pp. 3750–3759, Apr 1996.

[39] E. Cerda and L. Mahadevan, "Conical surfaces and crescent singularities in crumpled sheets," *Physical Review Letters*, vol. 80, no. 11, pp. 2358–2361, 1998.

[40] A. Lobkovsky, S. Gentges, H. Li, D. Morse, and T. Witten, "Scaling properties of stretching ridges in a crumpled elastic sheet," *Science*, vol. 270, no. 5241, pp. 1482–1485, 1995.

[41] A. Lobkovsky and T. Witten, "Properties of ridges in elastic membranes," *Physical Review E*, vol. 55, no. 2, p. 1577, 1997.

[42] S. Chaïeb, F. Melo, and J. Géminard, "Experimental study of developable cones," *Physical Review Letters*, vol. 80, no. 11, pp. 2354–2357, 1998.

[43] E. Hamm, B. Roman, and F. Melo, "Dynamics of developable cones under shear," *Physical Review E*, vol. 70, no. 2, p. 026607, 2004.

[44] A. Boudaoud, P. Patrício, Y. Couder, M. Amar, *et al.*, "Dynamics of singularities in a constrained elastic plate," *Nature*, vol. 407, no. 6805, pp. 718–720, 2000.

[45] M. Amar and Y. Pomeau, "Crumpled paper," *Proceedings of the Royal Society of London. Series A: Mathematical, Physical and Engineering Sciences*, vol. 453, no. 1959, pp. 729–755, 1997.

[46] L. Pauchard and S. Rica, "Contact and compression of elastic spherical shells: the physics of a 'ping-pong'ball," *Philosophical Magazine B*, vol. 78, no. 2, pp. 225–233, 1998.

[47] C. Quilliet, C. Zoldesi, C. Riera, A. Van Blaaderen, and A. Imhof, "Anisotropic colloids through non-trivial buckling," *The European Physical Journal E: Soft Matter and Biological Physics*, vol. 27, no. 1, pp. 13–20, 2008.

[48] S. Knoche and J. Kierfeld, "Buckling of spherical capsules," *Physical Review E*, vol. 84, p. 046608, Oct 2011.

[49] C. Quilliet, "Numerical deflation of beach balls with various poisson's ratios: from sphere to bowl's shape," *The European physical journal. E, Soft matter*, vol. 35, no. 6, p. 9725, 2012.

[50] S. Komura, K. Tamura, and T. Kato, "Buckling of spherical shells adhering onto a rigid substrate," *The European Physical Journal E: Soft Matter and Biological Physics*, vol. 18, no. 3, pp. 343–358, 2005.

[51] A. Vaziri, "Mechanics of highly deformed elastic shells," *Thin-Walled Structures*, vol. 47, no. 6-7, pp. 692–700, 2009.

[52] H. Ruan, Z. Gao, and T. Yu, "Crushing of thin-walled spheres and sphere arrays," *International journal of mechanical sciences*, vol. 48, no. 2, pp. 117–133, 2006.

[53] X. Dong, Z. Gao, and T. Yu, "Dynamic crushing of thin-walled spheres: An experimental study," *International Journal of Impact Engineering*, vol. 35, no. 8, pp. 717–726, 2008.

[54] S. N. Amiri and H. A. Rasheed, "Plastic buckling of thin hemispherical shell subjected to concentrated load at the apex," *Thin-Walled Structures*, vol. 53, no. 0, pp. 72 – 82, 2012.

[55] N. Gupta, G. Easwara Prasad, and S. Gupta, "Axial compression of metallic spherical shells between rigid plates," *Thin-walled structures*, vol. 34, no. 1, pp. 21–41, 1999.

[56] R. Kitching, R. Houlston, and W. Johnson, "A theoretical and experimental study of hemispherical shells subjected to axial loads between flat plates," *International Journal of Mechanical Sciences*, vol. 17, no. 11, pp. 693–703, 1975.

[57] A. Nasto, A. Ajdari, A. Lazarus, A. Vaziri, and P. M. Reis, "Localization of deformation in thin shells under indentation," *Soft Matter*, 2013.

[58] R. W. Ogden, *Non-linear elastic deformations*. Courier Dover Publications, 1997.

[59] L. Landau and B. Levich, "Dragging of a liquid by a moving plate," *Acta Physiochim*, vol. 17, pp. 42–54, 1942.

[60] F. Penning, "Nonaxisymmetric behavior of shallow shells loaded at the apex.," 1966.

[61] J. R. Fitch, "The buckling and post-buckling behavior of spherical caps under concentrated load," *International Journal of Solids and Structures*, vol. 4, no. 4, pp. 421–446, 1968.

[62] D. Vella, A. Ajdari, A. Vaziri, and A. Boudaoud, "The indentation of pressurized elastic shells: from polymeric capsules to yeast cells," *Journal of The Royal Society Interface*, vol. 9, no. 68, pp. 448–455, 2012.

[63] M. A. Dias, L. H. Dudte, L. Mahadevan, and C. D. Santangelo, "Geometric mechanics of curved crease origami," *Physical Review Letters.*, vol. 109, p. 114301, Sep 2012.

[64] A. Pocheau and B. Roman, "Uniqueness of solutions for constrained elastica," *Physica D: Nonlinear Phenomena*, vol. 192, no. 3â"4, pp. 161 – 186, 2004.

[65] B. Roman and A. Pocheau, "Postbuckling of bilaterally constrained rectangular thin plates," *Journal of the Mechanics and Physics of Solids*, vol. 50, no. 11, pp. 2379–2401, 2002.

[66] J. G. De Oliveira and T. Wierzbicki, "Crushing analysis of rotationally symmetric plastic shells," *The Journal of Strain Analysis for Engineering Design*, vol. 17, no. 4, pp. 229–236, 1982.

[67] J. D. Holmes, *Wind loading of structures.* Taylor & Francis, 2001.

[68] D. Vella, A. Ajdari, A. Vaziri, and A. Boudaoud, "Wrinkling of pressurized elastic shells," *Physical Review Letters.*, vol. 107, p. 174301, Oct 2011.